Imaging the Tumor Microenvironment

15

Marie-Caline Z. Abadjian, W. Barry Edwards, and Carolyn J. Anderson

15.1 Introduction

The microenvironment of solid tumors is heterogeneous and complex, and consists of cancer, stromal and immune cells [1], as well as areas of necrosis [2] (Fig. 15.1). The process of cancer metastasis is highly dependent on the microenvironment of both the primary tumor, as well as the connective tissue stroma at the site of future metastasis, as tumor cells interact with the endothelium of this organ [3]. Inflammation plays a major role in cancer development, which has been viewed as a dysregulated form of protective tissue repair and growth response [4]. Leukocyte infiltration in tumors, including macrophages and neutrophils, is now well known to be one of the "hallmarks of cancer" [1], and can exert both tumor-suppressive and tumor-promoting effects [4]. There is broad diversity of imaging biomarkers for many aspects of the tumor microenvironment. Specific imaging of the cell types and/or physiological factors in the microenvironment can provide critical information regarding cancer aggressiveness and response to treatment. This chapter will discuss several approaches utilizing a multitude of modalities that have been investigated for imaging the tumor microenvironment in mouse models and in humans.

15.2 Imaging Tumor-Associated Inflammation

It has long been known that some tumors are densely infiltrated by cells of both the innate (e.g. macrophages, neutrophils) and adaptive (e.g. T-cells) arms of the immune system [5]. It is now accepted that virtually every tumor contains immune cells at some level, ranging from barely detectable by immunohistochemistry to gross inflammation that can be imaged by standard histology [1, 6] and in vivo imaging [7]. It has also

M.-C.Z. Abadjian
Department of Medicine, University of Pittsburgh, Pittsburgh, PA, USA
e-mail: mca38@pitt.edu

W.B. Edwards
Department of Radiology, University of Pittsburgh, Pittsburgh, PA, USA

Department of Bioengineering, University of Pittsburgh, Pittsburgh, PA, USA
e-mail: edwardsw@upmc.edu

C.J. Anderson (✉)
Department of Pharmacology & Chemical Biology, University of Pittsburgh, Pittsburgh, PA, USA

Department of Medicine, University of Pittsburgh, Pittsburgh, PA, USA

Department of Radiology, University of Pittsburgh, Pittsburgh, PA, USA

Department of Bioengineering, University of Pittsburgh, Pittsburgh, PA, USA
e-mail: andersoncj@upmc.edu

P. Kalinski (ed.), *Tumor Immune Microenvironment in Cancer Progression and Cancer Therapy*, Advances in Experimental Medicine and Biology 1036,
https://doi.org/10.1007/978-3-319-67577-0_15

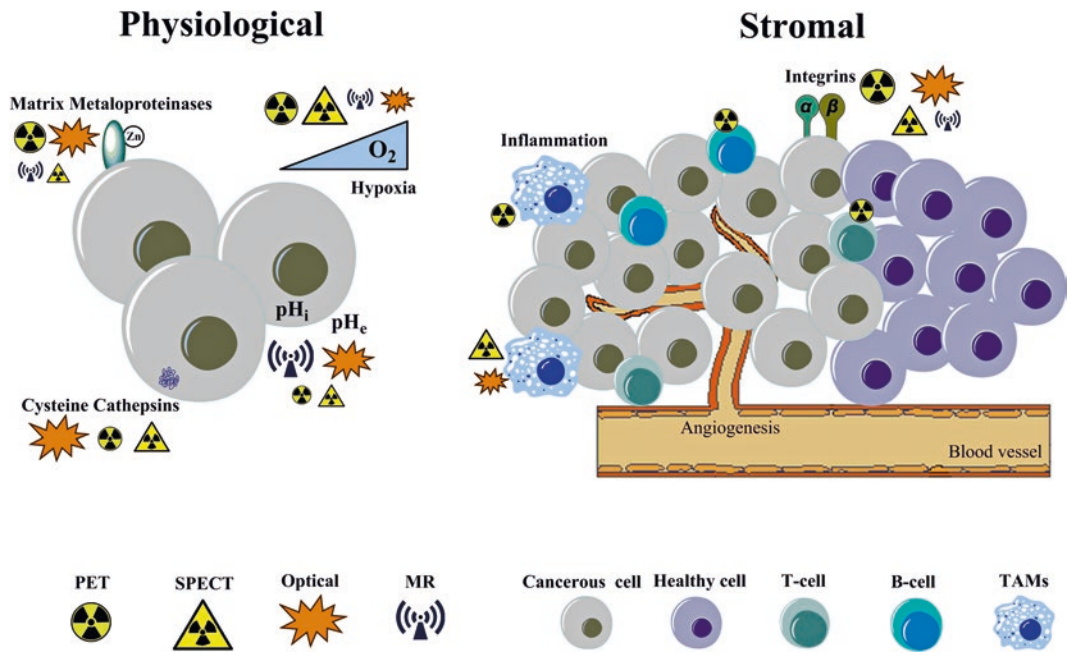

Fig. 15.1 Physiological and stromal factors are targeted to image the tumor microenvironment by various modalities. Unique components of the tumor microenvironment include: hypoxia, internal and external pH ratios, enzymes such as matrix metaloproteinases and cysteine cathepsins, as well as integrins, tumor-associated macrophages which induce angiogenesis and inflammation, respectively

been shown that neutrophils, activated macrophages and dendritic cells (DCs) are present at the tumor margins [8]. Inflammation brings bioactive molecules to the tumor microenvironment, including growth and survival factors that promote tumor cell growth, and matrix-modifying enzymes that contribute to angiogenesis, invasion and metastasis [9–11]. Inflammation may also be causative in promoting the transformation of early neoplasias to fully developed cancer [11]. In vivo imaging of various aspects of inflammation in cancer is vitally important, and can aid in the early diagnosis of tumor growth and progression. In this section we will discuss imaging of tumor-associated macrophages (TAMs) and T-cells that have roles in both cancer progression and regression.

Macrophages in cancer. Monocytes, which originate in bone marrow and spleen, are recruited to tumors by tumor-derived chemokines and growth factors where they differentiate in macrophages [12]. M1 polarized macrophages benefit the host by mediating a classical inflammatory response against such pathogens as bacteria and viruses and can act as antigen presenting cells for antibody production against foreign proteins [13]. They also have a protective role in tumors and suppress the activities of tumor promoting cells [14]. However, recent evidence has emerged that in cancer, M2 polarized macrophages promote tumor growth. For example, TAMs have an M2 phenotype and secret enzymes that remodel the extracellular matrix and promote metastasis. They also suppress the adaptive immune response. Moreover, high numbers of TAMs in tumors have been linked to low survival rates [15]. Therefore, non-invasive diagnostic imaging of TAMs could have prognostic power to stratify patients for therapy. Because a characteristic of macrophages is there ability phagocytose large particles, a particularly attractive approach is to use both non-targeted and targeted nanoparticles [16].

Non-targeted nanoparticles. To take advantage of the phagocytotic activity of M2-polarized macrophages, non-targeted nanoparticles have

been investigated (Fig. 15.2). In one approach, radiolabeled high-density lipoprotein based nanoparticles (rHDL) incorporating the long-lived positron-emitting nuclide ^{89}Zr and a NIR dye (DiO) were developed [17]. These nanoparticles were composed of phospholipids and apolipoprotein. When injected into tumor-bearing mice, histologic analysis of tumor tissues was consistent with particle accumulation in TAM dense tumor regions. By changing the conjugation site of the ^{89}Zr chelator, DFO, to either a phospholipid or to apoA-I, different biodistributions were observed. Moreover, disaggregated tumors showed the greatest uptake of the particles in TAMs with lower accumulation in dendritic cells and in the tumor cells, although macrophage targeting was not exclusive. That lack of exclusivity was attributed to unanticipated particle interaction with the different cell types.

Targeted nanoparticles. To enhance efficiency of nanoparticle uptake in TAMs, they can be conjugated with ligands that are targeted to cell surface receptors on macrophages. In an example of this approach, ^{64}Cu- and DiO-labeled

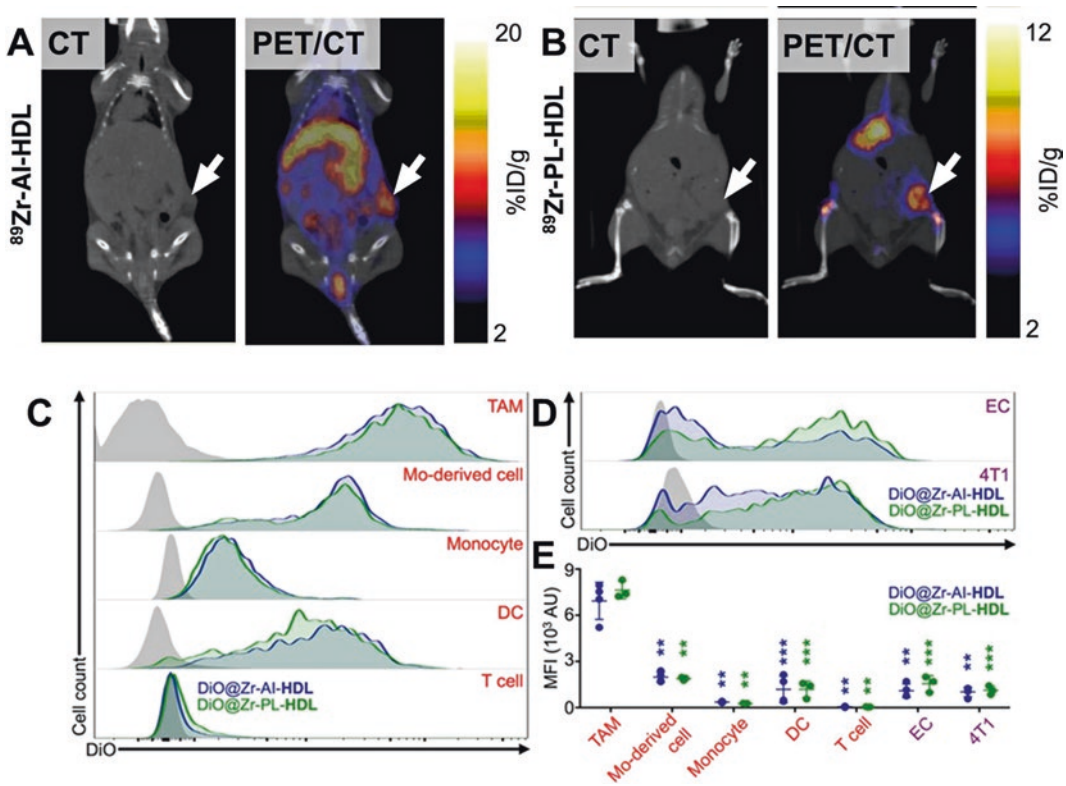

Fig. 15.2 ^{89}Zr-labeled high-density lipoprotein based nanoparticles incorporate in M2-polarized macrophages by phagocytosis in orthotopic 4T1 mouse mammary tumor-bearing mice. *Top* Accumulation of ^{89}Zr-HDL nanotracers in tumor tissues can be visualized by in vivo PET imaging. CT (*left*) and PET/CT fusion (*right*) images of ^{89}Zr-AI-HDL (**a**) and ^{89}Zr-PL-HDL (**b**) obtained at 24 h after injection in mice bearing orthotopic 4T1 tumors (indicated by *arrows*). *Bottom* Both DiO@Zr-PL-HDL and DiO@Zr-AI-HDL preferentially target tumor-associated macrophages. 4T1 cell–induced orthotopic breast tumors were used to isolate single cells. (**c**) Representative DiO levels in five immune cells, namely TAMs, monocyte-derived cells (Mo-derived cells), monocytes, dendritic cells (DCs), and T cells. (**d**) Representative DiO levels in ECs and tumor cells (4T1). Cells from a phosphate-buffered saline-injected mouse served as controls (*gray* histograms to *left*). (**e**) Quantification of DiO levels presented as mean fluorescence intensity (MFI). Importantly, no statistical significance was found when comparing DiO levels of same cell type from two HDL formulations. Statistics were calculated with 2-tailed Student t test with unequal variance by comparing with TAM from same group. **P < 0.01. ***P < 0.001. Adapted from reference [17]

mannose coated liposomes were used to target mannose receptors (CD206) overexpressed on TAMs in lung tumors induced through chemical treatment [18]. Evidence for mannose-mediated uptake was that targeted accumulation in both tumor and spleen exceeded non-target accumulation and that confocal microscopy of lung tissue sections demonstrated co-localization of DiO-labeled liposomes and a pan macrophage marker F4/80.

Molecular imaging agents for macrophages. CD206 has also been targeted with non-nanoparticle molecular imaging agents [19]. A nanobody (Nb cl1) against CD206 radiolabeled with ^{99m}Tc was investigated for visualizing macrophages in tumor bearing mice, both wild type and CD206 knock out mice, and a non-binding control (BCII10) was included. The in vivo results in mice bearing 3LL tumors showed there was no uptake of the CD206 targeted ^{99m}Tc-Nb cl1 in the CD206 knockout mice, demonstrating that the tumor itself does not express significant levels of CD206. However, in WT mice, the targeted antibody localized to the tumor as well as tissue resident macrophages in the liver. The non-binding control did not accumulate significantly in CD206 enriched tissues, which demonstrates CD206 mediated accumulation. Numerous ex vivo experiments supported CD206 mediated accumulation of Nb cl1 including localization of AF647-Nb cl1 in tumor tissue that co-stained with F4/80, a pan macrophage marker.

CD11b is a marker for macrophages as well as dendritic cells but may not exclusively mark M2-polarized macrophages. An ^{18}F-labeled variable heavy chain (VHH) raised against CD11b, readily visualized tumor associated inflammation in a syngeneic mouse model of melanoma (B16F10) by small animal PET, whereas ^{18}F-FDG failed to generate a clear delineation of the tumor [7]. Ex vivo two-photon microscopy demonstrated that the dye-conjugated anti-CD11b VHH had high uptake in CD11b enriched lymphoid organs and virtually no uptake in the corresponding knock-out mice thus supporting the specific high uptake observed in vivo. Flow cytometry of the disaggregated tissues stained with the dye-labeled anti-CD11b VHH were consistent with the findings of the microscopy.

Molecular imaging agents for T-cells. Imaging CD8-expressing cells will be important to track T-cells for non-invasive monitoring of these populations during immunotherapy [20]. Utilizing known sequences for murine CD8 monoclonal antibodies, minibodies (Mbs) were constructed. The Mbs retained high affinity for CD8 and readily stained disaggregated CD8 positive cells from thymus, spleen, and lymph nodes. Unlike the parental antibodies, the Mbs did not deplete T-cells from the host mice. After Cu-64 labeling, uptake in CD8+ tissues was readily visualized by preclinical PET. Uptake was clearly visualized in lymph nodes and spleen (Fig. 15.3) 4 h post injection.

15.3 Imaging Hypoxia in the Tumor Microenvironment

Hypoxia (low oxygenation) occurs in the tumor microenvironment where cells are rapidly growing and taxing the oxygen availability from its surrounding blood supply [21–23]. Chronic and acute/cycling hypoxia are two categories found in the tumor microenvironment [24–26]. Chronic hypoxia arises from diffusion limited oxygen availability, and acute hypoxia occurs from transient perfusion disruptions. In both cases, the oxygen supply is reduced compared to normal supply (normoxia). There are several reviews on different modes of imaging probes targeting hypoxia to study the tumor microenvironment, which include polarographic O_2 microelectrodes, various positron emission tomography (PET) and single photon emission computed tomography (SPECT) tracers, magnetic resonance imaging (MRI) methods and fluorescence probes [27–31]. PET tracers for imaging hypoxia have had much success in the clinic and have been compared amongst each other [32–38]. Recently investigated imaging probes targeting hypoxia in the tumor microenvironment will be discussed.

PET/SPECT tracers for hypoxia imaging: Huang et al. compared ^{18}F-labeled 2-deoxyglucose

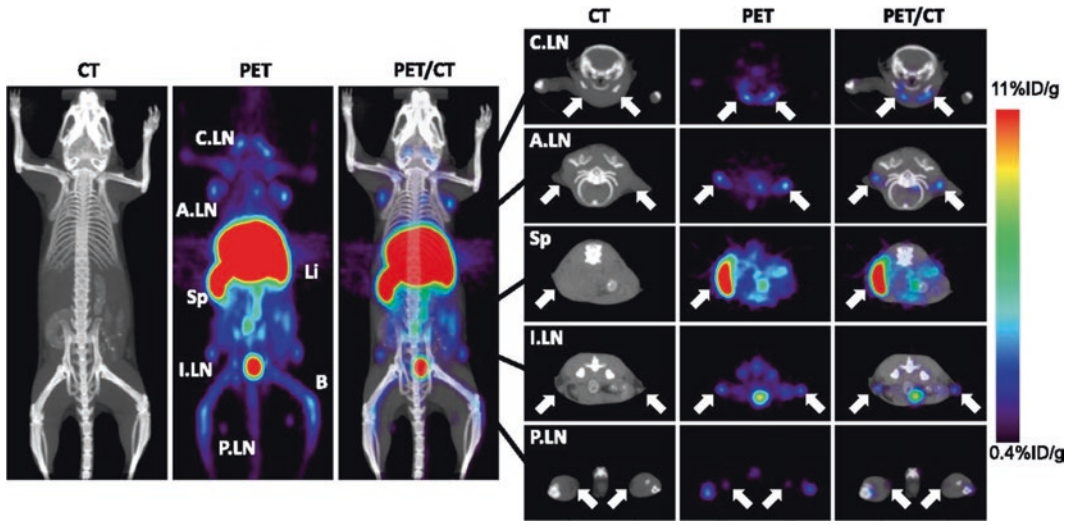

Fig. 15.3 Immuno-PET imaging of CD8 positive T-cells with ^{64}Cu-NOTA-2.43 Mb was observed in thymus, spleen and lymph nodes 4 h after i.v. injection in B/6 mice. The white arrows (2-mm transverse MIPs) are used to highlight uptake in various lymph nodes (*right*) and the spleen seen in the whole-body 20-mm coronal MIPs (*left*). *A.LN* axillary lymph nodes; *B* bone, *C.LN* cervical lymph nodes, *I.LN* inguinal lymph nodes, *Li* liver, *MIPs* maximum intensity projections, *P.LN* popliteal lymph nodes, *Sp* Spleen. Adapted from reference [20]

(FDG), 3′-deoxy-3′-[^{18}F]fluorothymidine (FLT) and 1-(2-nitroimidazolyl)-3-[^{18}F]fluoro-2-propanol (FMISO) distribution in subcutaneously implanted and disseminated peritoneal NSCLC A549 and HTB177 tumors in mice by digital autoradiography and compared this to immunohistochemistry images of tumor hypoxia, proliferation, stroma and necrosis [2]. The accumulation of FDG and FLT were broadly similar for both cell lines and for subcutaneous and disseminated tumors. FDG was found to have higher uptake in regions of high pimonidazole binding (hypoxia), although there were some mismatched regions. Areas of higher FDG activity tended towards low proliferation and perfusion, while stroma and necrotic areas showed lower FDG uptake. FLT accumulation in the tumor correlated with high uptake of bromodeoxyuridine and negative staining for pimonidazole, and showed low uptake in stroma and necrosis. As expected, FMISO activity correlated with pimonidazole binding in A549 s.c. tumors, corresponding to low proliferation and perfusion. Stroma and necrotic areas of the tumor had low FMISO accumulation. Generally speaking, FDG and FMISO are similar in areas of hypoxia, stroma and necrosis, whereas FLT better images non-hypoxic regions of the tumor.

A limitation to be considered when imaging with PET tracers is the uptake time, as it influences the lesion-to-background ratio as well as the signal-to-noise ratio. The most widely used hypoxia imaging PET tracer is FMISO [39, 40]. In humans, FMISO was found to give better quality images of hypoxic tumors at 4 h compared to 2 h [41]. Additional studies have shown an accurate reflection of hypoxia detected by FMISO and expression of hypoxia-inducible factor 1α (HIF-1α) and vascular endothelial growth factor (VEGF) in 32 patients with gliomas [42]. FMISO also images hypoxia in micrometastases growing in mice xenograft models of human non-small cell lung cancer (NSCLC) A549 and HTB177 cells [43]. Other F-18 labeled PET tracers like 3-^{18}F-fluoro-2-(4-((2-nitro-1-himidazol-1-yl)methyl)-1H-1,2,3,-triazol-1-yl)-propan-1-ol (^{18}F-HX4) and ^{18}F-fluoroazomycin arabinoside (^{18}F-FAZA) also were found to image hypoxia in NSCLC patients [44, 45] and mice bearing human SiHa cervix tumor xenografts [46]. Comparisons have been done of FMISO, ^{18}F-HX4 and ^{18}F-FAZA in rhabdomyosarcoma

R1-bearing WAG/Rij rats evaluating optimal time to image, tumor-to-blood ratios, spatial reproducibility, and sensitivity to oxygen changes [47]. The comparisons found each F-18 PET tracer had advantages, which could be capitalized upon depending on the imaging requirements. FMISO has also been compared with FDG in patients with pancreatic adenocarcinoma, although there was no significant correlation between SUV_{max} for the two tracers [48]. FMISO was also compared to ^{18}F-HX4 in hypoxia imaging in heat and neck cancer patients, and tumor-to-muscle ratios were similar for both imaging probes [49].

Another F-18 PET hypoxia imaging probe is ^{18}F-fluoroerythronitroimidazole (^{18}F-FETNIM), which has been studied in patients with NSCLC. Tumor-to-mediastinum (T/Me) ratios were quantified on PET/CT and correlated with expression of HIF-1α, glucose transporter 1 (GLUT-1) and VEGF [50]. ^{18}F-FETNIM hypoxia imaging was used to determine a hypoxia threshold, quantifying variability in untreated esophageal squamous cell carcinoma (SCC) in patients, and evaluating clinical response after concurrent chemoradiotherapy [51]. Overall ^{18}F-FETNIM PET/CT showed similar uptake in esophageal SCC and baseline SUV_{max} might have predictive value. Preliminary results for a modified version of this ^{18}F hypoxia imaging probes were investigated; a sulfoxide derivative, (^{18}F-F1) was imaged in vitro (S9 liver homogenate fractions) and in vivo (SK-RC-52 tumor model BALB/c nude mice) and found to have good retention in tumors [52].

^{18}F-labeled PET hypoxia imaging probes have also been examined for detecting changes before and during treatment. ^{18}F-FAZA was used to successfully identify and quantify tumor hypoxia before and during concurrent chemoradiotherapy in patients with advanced head and neck SCC [53]. In a handful of studies, FMISO PET imaging was shown to have prognostic value used to evaluate hypoxia tumors' microenvironment after treatment [54–56].

Other radionuclides have been used to image hypoxia in the tumor microenvironment such as ^{99m}Tc, ^{62}Cu, ^{64}Cu, ^{67}Ga, and ^{68}Ga. Current findings will be briefly presented. A ^{99m}Tc-pyrimidine-4,5-diamine (^{99m}Tc-PyDA) was developed and studied in vitro stability and in vivo hypoxia targeting [57]. In vivo studies with ^{99m}Tc-PyDA in mice with injected with Ehrlich ascites carcinomas showed selective uptake in hypoxia tumor tissues. Derivatives of metronidazole (4-isocyano-N-[2-(2-methyl-5-nitro-1H-imidazol-1-yl)ethyl]butanamide (M1) and 1-(4-isocyanobutanoyl)-4-[2-(2-methyl-5-nitro-1H-imidazol-1-yl)ethyl]piperazine (M2)) have also been investigated as ^{99m}Tc tracers (^{99m}Tc-NS3M1 and ^{99m}Tc-NS3M2) for imaging hypoxia in mice bearing induced 3LL Lewis murine lung carcinoma [58]. Tracer ^{99m}Tc-NS3M1 was found to have favorable tumor-to-muscle ratio in vivo. Another SPECT tracer, ^{99m}Tc-meropenem was demonstrated to have higher selectivity in tumor hypoxia tissue compared to ^{18}F -FDG-PET and ^{99m}Tc-nitroimidazole, and was also shown to differentiate from inflamed and infected tissues in mouse models [59]. A bioreductive ^{99m}Tc hypoxia imaging probe (^{99m}Tc-SD32) was found to be retained in FM3A murine breast tumor cells under hypoxic compared to normoxic conditions [60].

Copper-64, Cu-60 and Cu-62 have been used to make PET hypoxia imaging probes. Patients with glioma were imaged with ^{62}Cu-diacetyl-bis (N4-methylthiosemicarbazone) (^{62}Cu-ATSM) to distinguish tumor grades and tissue hypoxia correlated well to MR imaging and HIF-1α expression [61]. ^{64}Cu-ATSM autoradiography and PET were compared with FDG PET in spontaneous canine sarcomas and carcinomas [62, 63]. Correlations between ^{64}Cu-ATSM and ^{18}F-FDG PET were found at later time points (3 hours post injection), and similar distribution in heterogeneous tumor regions were found for ^{64}Cu-ATSM autoradiography and pimonidazole immunohistochemistry. The well-known ^{64}Cu-ATSM and ^{18}F-FMISO have been compared under several conditions and hypoxia tumor types, findings have noted advantages in both [64]. Derivatives of ^{64}Cu-ATSM have been investigated in EMT6 carcinoma cells; revealing an imagine probe (^{64}Cu-ATSM/en) with higher hypoxia selectivity and lower non-target organ uptake than

^{64}Cu-ATSM in EMT6 tumor-bearing mice [65]. ^{60}Cu-ATSM has also been investigated in women with cervical cancer, and was found to be a predictor of recurrence [66].

Gallium-68 and Ga-67 nitroimidazole and metronidazole derivatives have also been used as PET/SPECT imaging probes for hypoxia. One nitroimidazole derivative, ^{68}Ga-HP-DO3A-nitroimidazole (^{68}Ga-HP-DO3A-NI), was studied in vitro in A549 lung cancer cells and in vivo in SCID mice with A549 tumor xenografts [67]. ^{68}Ga-HP-DO3A-NI showed favorable pharmacokinetics with little accumulation in liver, heart or lung, and selectivity for hypoxic tissue compared to controls. Two metronidazole derivatives (^{67}Ga-DOTA-MN1 and ^{67}Ga-DOTA-MN2) were investigated [68]. ^{67}Ga-DOTA-MN2 showed higher accumulation and selectivity in vivo (NFSa mouse fibrosarcoma or FM3A cells inoculated s. c. in female C3H/He mice) compared to controls and ^{67}Ga-DOTA-MN1); ^{68}Ga-DOTA-MN2 was successfully imaged at 1 h by small-animal PET. In another study, ^{68}Ga-DOTA conjugated to nitroimidazole (amide bond, ^{68}Ga-4; thiourea bond, ^{68}Ga-5) were explored and ^{68}Ga-5 was found to have higher uptake in vitro cancer cell lines (HeLa, CHO, and CT-26) than ^{68}Ga-4 [69]. Interestingly, in mice xenografted with CT-26 mouse colon cancer cells, ^{68}Ga-4 had higher standard uptake values (SUV) in tumors than ^{68}Ga-4.

MR contrast agents for imaging hypoxia. Although not as prevalent as for PET, MRI contrast agents have been developed to image hypoxia in vivo (Fig. 15.4) [70, 71]. MRI for hypoxia imaging has mainly utilized dynamic contrast-enhanced magnetic resonance imaging (DCE-MRI). DCE-MRI has been shown to analyze areas of hypoxia in tumors in vitro or in vivo [72–74].

Optical probes for imaging hypoxia. Optical imaging of hypoxia in the tumor microenvironment has been investigated with various probes [75, 76]. Nanoparticles (NPs), including polystyrene NPs and boron NPs have been explored [77, 78]. Fluorescent, phosphorescent, and Förster energy transfer (FRET) off-on probes have also been developed to explore imaging hypoxic microenvironments [79, 80]. Ruthenium (Ru) and iridium (Ir) complexes are intriguing phosphorescent hypoxia imaging probes that offer real-time imaging. Ruthenium complexes containing nitroimidazole (Ru-NI1) can monitor oxygen fluctuations in vitro (A549 human lung adenocarcinoma epithelial cells) and in vivo (A549 cells injected s.c. in female BALB/c nu/nu mice) [81]. Other ruthenium complexes like $[Ru(dpp)_3]^{2+}Cl_2$ NPs have successfully imaged

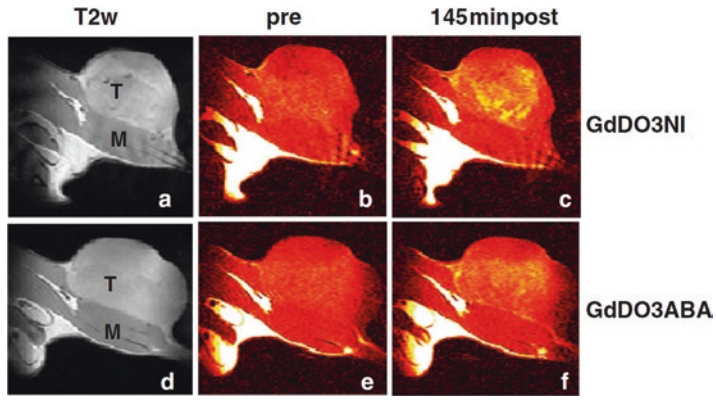

Fig. 15.4 T2-weighted MRI imaging of hypoxia was performed in Dunning prostate R3327-AT1 tumor-bearing rats. Grayscale magnetic resonance T2-weighted (**a**, **d**) and color T1-weighted (**b**, **c**, **e**, **f**) images of Copenhagen rat thighs bearing syngeneic Dunning prostate R3327-AT1 tumors following injection of 0.1 mmol GdDO3NI per kilogram body weight (**a**–**c**) or 0.1 mmol GdDO3ABA per kilogram body weight (**d**–**f**) before injection (**b**, **e**) and 145 min after injection (**c**, **f**). The tumor and thigh muscle are labeled T and M, respectively [70]

hypoxia in U87MG cells and zebrafish embryos [82]. Ruthenium complexes comprised of hydrophobic components like pyrene (Ru-Py) also exhibited hypoxia selective imaging in A549 cells and in female BALB/cSlc nu/nu mice [83]. Although not as common, iridium complexes ($Ir(btp)_2acacBTP$) were found to image hypoxia in vitro (HeLa, CHO, SCC-7, U251) and in vivo tumor-bearing (SCC-7, U87, RAMOS, HT-29, LL-2) female athymic nude mice [84].

15.4 Imaging pH Changes in Tumor Cells and the Microenvironment

The acidic pH found in the tumor microenvironment has been attributed to the fast cell growth and division, which consumes oxygen and nutrients. Tumor cells adapt to the resulting anaerobic conditions producing lactic acid that ultimately affects the intracellular and extracellular pH. The elevated intracellular pH (pH_i) from glycolysis triggers efflux of lactate and protons via monocarboxylate transporters and Na-driven proton extrusion resulting in decreased extracellular pH (pH_e) [85, 86]. Diseased tissue has been shown to have lower local pH_e ranges (5.66–7.78) than normal tissues (7.4) [87, 88]. In normal cells, pH_i is lower than pH_e, but in cancer cells the pH gradient is reversed and stimulates cancer progression and cellular function [89]. Targeting low pH is another characteristic utilized to image the tumor microenvironment.

In the early 1980s, tumor pH measurements were done with pH electrodes, but tissue and capillary damage from probe insertion as well as loss of sensitivity in finer probes led to the development of other non-invasive probes [90–92]. The characteristics of an ideal pH probe are (1) the probe should exist in ionized and unionized forms, where the ratio of the two forms are proportional at the pH of interest; (2) the probe should not change tissue pH; (3) tissue compartmentalization of the probe should be known; (4) the probe should be nontoxic; (5) the measurements of pH should be independent of probe concentration; and (6) pH measurements should be rapid such that temporal changes in pH can be measured [93]. Currently, various pH probes generally use the physical properties of acidic protons for MRS and MRI, acid-cleavability (pH-activatable) for fluorescent probes and pH (low) insertion peptide (pHLIP®) for SPECT/PET tracers.

MRI probes for imaging pH changes. Hyperpolarized nuclei increase sensitivity of NMR and MRI experiments, and hyperpolarized ^{13}C and ^{89}Y have been used for in vitro and in vivo mapping of pH in normal and inflammation mouse models [86, 94, 95]. Chemical exchange saturation transfer (CEST) is a common MRI technique that selectively saturates exchangeable protons that are transferred to bulk water signal [96]. Biosensor imaging of redundant deviations in shifts (BIRDS) which measures exchangeable protons like $-OH$ and $-NH_y$, where $2 \geq y \geq 1$, was compared with CEST for pH imaging [97]. BIRDS showed good sensitivities, eliminating the need to use water resonance as a reference thereby offering a new method to calibrate CEST. AcidoCEST is a known MRI technique to measure acidosis within tumors. Several groups have measured tumor pH_e using acidoCEST MRI in conjunction with the repurposed CT contrast agents, iopromide and/or iopamidol. In vivo studies in xenograft tumor models of Raji lymphoma and MCF-7 breast cancer showed iopromide to measure a greater tumor region compared to iopamidol [98]. Processing methods were evaluated in acidoCEST MRI with iopromide, finding MCF-7 to be more acidic than MDA-MB-231 tumor models in mice [99]. A CEST-fast imaging with steady-state free precession (FISP) method was successfully used to detect iopromide in the MDA-MB-231 mouse model, and tumor pH_e monitored after bicarbonate treatment [100]. Iopamidol has also been used in CEST MRI to generate pH maps in vivo (mouse model of acute kidney injury) over 21 days; the study was able to differentiate among functional regions of damaged kidneys [101]. A ratiometric CEST imaging method using iobitridol, an X-ray contrast agent, has been developed under different radiofrequency (RF) irradiation power levels in vitro and in vivo (xenografted adenocarcinoma TSA tumors s.i. in mouse model) [102]. The RF power-based ratiometric pH MRI method improves in vivo pH sensitivity in pH imaging.

Paramagnetic chemical exchange saturation transfer (PARACEST) is another MRI technique using paramagnetic lanthanides designed with chelator groups that are CEST selective such that the ratio of the two CEST effects can be used to remove the influence of concentration in the pH measurements [103]. PARACEST and CEST-FISP MRI were successfully used in combination to detect pH_e in tumor tissue (MDA-MB-231 mammary carcinoma and MCF-7) in vivo using Yb-DO3A-oAA [104, 105]. A glycol chitosan (GC) with pH-titratable primary amines coupled to Gd-DOTA (GC-NH_2-GdDOTA) has shown in vitro and in vivo (T6–17 cells injected into nu/nu nude mice) provided diagnostic information about the tumor environment while giving high spatiotemporal resolution [106]. A variety of pH probes have been developed using MRI to image the tumor microenvironment. Representative pH_e probes also include mixed micelles that are destabilized at different pH, which can generate pH maps of solid tumors in vivo [107], manganese oxide-based hybrid mesoporous composite nanocapsules for pH-responsive imaging as well as ultrasonography in vitro and in vivo [104], and glycol chitosan coupled to superparamagnetic iron oxide nanoparticles (SPIO) that associates with tumor tissues in vivo [108]. Dual imaging pH probes have also been advanced to image the tumor microenvironment. One example is lanthanide complexes (DO3A) conjugated to rhodamine that gives higher fluorescence at lower pH due to ring opening of the spirolactam while providing MR images [109]. In vitro studies in HEK293 cells and primary mouse islet cells demonstrated the dual MR/fluorescent probe to distinguish between tumor and healthy cells as well as in vivo images from BALB/c nude mice bearing M21 melanoma xenografts.

Fluorescent probes for imaging pH changes. Fluorescence imaging of pH in the tumor microenvironment has seen a boon in the last decade. Several exciting pH probes have been explored. A near-infrared (NIR) fluorescent probe containing a hemicyanine (NIR-Ratio-BTZ) can be protonated/deprotonated on the hydroxyl group to give two photostable, sensitive, ratiometric and reversible states for imaging pH_i in real-time in vitro (HeLa cells) and in vivo (nude mice with LPS-mediated inflammatory response) [110] (Fig. 15.5). Water soluble naphthalene diimides (NDIs), which do not emit as a free base but strongly emit once protonated, were tested in vitro (PC-3 cells) and showed successful imaging of pH_i in tumor microenvironments [111]. A pH probe that has two NIR fluorophores coupled by an acid cleavable linker (DilRB-S) was investigated for visualizing tumors by imaging pH_e [112]. A high target-to-background ratio was obtained for DilRB-S in vivo (HCCLM3-GFP and HepG2 cells inoculated in male nude mice) and gave insight in evaluating metastatic potential of tumors studied. Another NIR ratiometric pH_i probe takes advantage of intramolecular charge transfer (ICT) with a coumarin-indole (π-bonded donor-acceptor) conjugate showing dual-emission changes with pH changes while imaging KB and HeLa cells [113].

Nanoparticles have been explored as a scaffold for pH probes. Gold nanoclusters protected by BSA (reference fluorophore) conjugated to fluorescein-isothiocyanate (response to pH) and folic acid (targeting folate acceptors on folic rich cancer cells) were studied to develop ratiometric pH_i probes for in vitro imaging (HeLa cells and lung cell carcinoma cells A549) [114]. Multifunctional nanoparticles (MNPs) made of silica coated iron oxide with benzo[a]phenoxazine (NIR dye) on the surface that fluorescence at pH lower than 6.0 were developed and tested in vitro (4T1 and 293T tumor cells) and in vivo to visualize the acidic tumor microenvironment with minimal toxicity [115]. An ultra pH-sensitive probe (UPS) was developed by conjugating a near-IR dye (Cy5.5) to a copolymer with cRGD targeting that self assembles into micelles [116]. These fluorescent pH probes have shown exponential nonlinear fluorescence activation at low pH indicative of the tumor microenvironment in vivo (nu/nu mice) in s.c. A549 lung carcinoma, MDA-MB-231 breast cancer, HN5 and HCC4034 head-neck cancer, SF-188 glioma, LN-229 glioma, 3LL lung carcinoma, Mia Paca-2 pancreatic cancer and PC-3 prostate tumors. Another micelle platform made from block copolymers (MPEG-PAE) with encapsulated fluores-

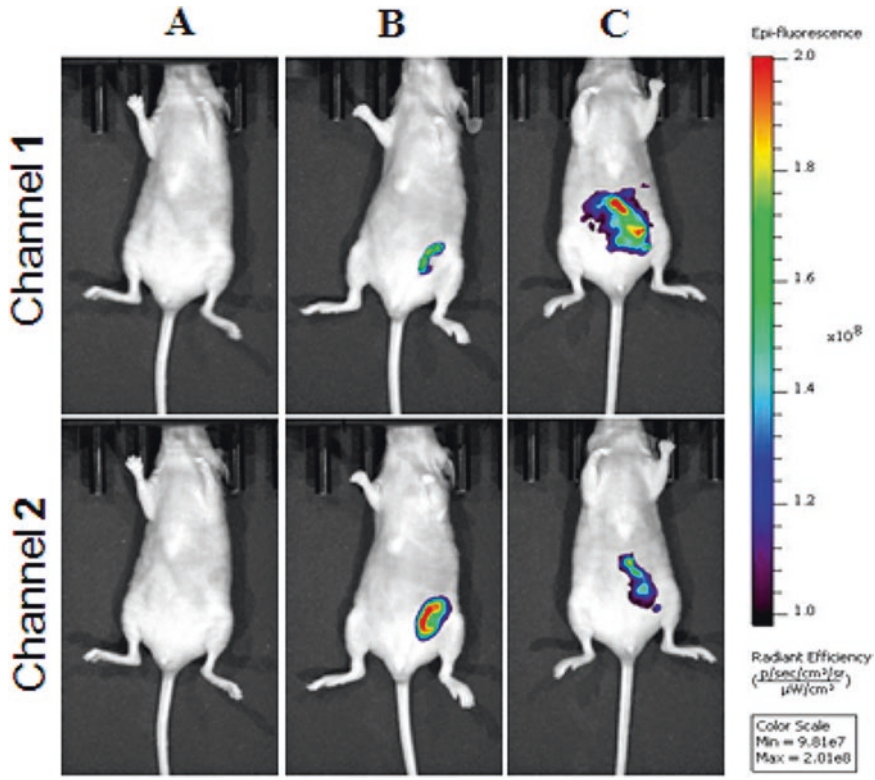

Fig.15.5 A near-infrared fluorescence probe with a hemicyanine dye that can be protonated or deprotonated on the hydroxyl group provides a ratiometric approach for imaging pH. Representative fluorescence images (*pseudocolor*) of mice injected with NIR-Ratio-BTZ during LPS-mediated inflammatory response in vivo. (**a**) Only LPS was injected for control. (**b**) Saline was injected in the peritoneal cavity of mouse, followed by injection of NIR-Ratio-BTZ (50 μM). (**c**) LPS was injected into the peritoneal cavity of the mouse, followed by injection with NIR-Ratio-BTZ (50 μM). The mice were imaged with an excitation filter 580 nm and two emission channels of Channel 1 (650 nm) and Channel 2 (720 nm) [110]

cent dye (TRITC) and black hole quencher (BHQ) have shown to break micelles at acidic pH with high tumor (MDA-MB-231 cells) specificity and sensitivity [117]. Biodegradable NIR fluorescence nanoprobes (InNP1 and Rd.-InNP1) for imaging acidic tumor microenvironments were shown to have high tumor-to-normal (T/N) ratio in vitro (human glioblastoma U87MG) and in vivo (s.c. U87MG tumor xenografts in female SCID mice) [118].

Another interesting platform for NIR fluorescent pH probes are quantum dots (QDs) decorated with fluorescent dyes. A quantum dot ($CuInS_2$/ZnS) surrounded by lauric acid and 2,3-dimethylmaleic anhydride modified ε-polylysine (QD@ε-PL-g-LA/DMA) exhibited a positive charge in acidic conditions and reverses to negatively charged at pH 7.4, showed proof of concept in HeLa cells [119]. Stable luminescent ZnSe/ZnS quantum dots conjugated with SNARF-5F fluorophore and porphyrins were explored with FRET demonstrating proof-of-concept for imaging pH in tumor microenvironment [120]. QD-mOrange-Arg9 and QD-mCherry-Arg9 dyes exhibited improved sensitivity and photostability to image pH_i in vitro (HeLa cells) compared to BCECF (commonly used fluorescent dye for pH imaging) [121]. In another study, nanogels with CdSe QDs in the interior of a polymer (hydroxypropylcellulose-poly(acrylic acid)) underwent pH dependent volume phase transition providing a low pH response for imaging [122]. Cellular imaging on mouse melanoma B16F10 cells with drug (temozolo-

mide) loaded nanogels gave a method to track release of drug with the low pH of the tumor microenvironment.

Ratiometric pH_i imaging was successfully performed by in HeLa Kyoto cells expressing SypHer2 (fluorescent indicator) in vitro and in vivo to compare to pathomorphology and hypoxia staining of tumors [123]. Another genetically encoded pH_i probe was a red fluorescent protein mKeima-A213S mutant (pHRed) notably imaged in vitro in Neuro2A cells expressing pHRed [124]. Photoacoutic nanoprobes have also been used to image the low pH of the tumor microenvironment. Mouse breast tumor model (EMT-6 cells) could be identified from normal tissue using a dextran based pH-sensitive near-IR nanoprobe [125]. In low pH environments, the nanoprobe's hydrazone bonds cleave causing the resonance absorption peaks in the near-IR region to change creating a different photoacoustic output.

PET imaging of acidic pH. A novel approach to imaging acidic pH in the tumor microenvironment was recently reported, where a pro-drug strategy was employed [126]. A caged derivative of FDG was developed, which is selectively degraded to the parent FDG upon exposure to acidic pH, allowing it to be taken up by adjacent cells. The acid labile pro-drug was based on the glycosylamine linkage, where cleavage is tunable based on the pK_a of the parent amine. In comparing PET imaging of a FDG-glyosylamine (FDG-amine 4; Fig. 15.6) with the parent FDG, only the tumor having an acidic microenvironment was imaged with FDG-amine 4, whereas with FDG other tissues that readily take up glucose were imaged (brain, heart, brown fat).

pHLIP probes. One type of acidic pH probe that has gained increased application in imaging the tumor microenvironment are pH (low) insertion peptides (pHLIPs) [127, 128]. Three fluorescently labeled pHLIPs (Alexa546-WT, Alexa546-Var3, Alexa546-Var7) have successfully accumulated in tumors of metastatic 4T1 mammary tumors and spontaneous breast tumors in FBV/N-Tg (MMTV-PyMT) 634Mul transgenic mice [129]. Fluorescently labeled pHLIPs have also been shown to localize and detect pancreatic ductal adenocarcinoma (PDAC), PDAC and PanIN lesions in human xenografts in mouse models [130]. Topical application of Alexa647 labeled pHLIPs in intact fresh human tissue specimens with head and neck squamous cell carcinoma have reported differences in clinically abnormal and normal tissues which concurred with pathologic evaluations [131]. pHLIPs have also been coupled to radiotracers for in vivo pH imaging with single-photon emission computed tomography (SPECT). Lewis lung carcinoma (LLC), lymph node carcinoma of the prostate (LNCaP) and prostate adenocarcinoma (PC-3) tumor xenografts in mice were studied using ^{99m}Tc-pHLIP (^{99m}Tc-AH114567) and showed adequate imageability and correlation with tumor extracellular acidity [132].

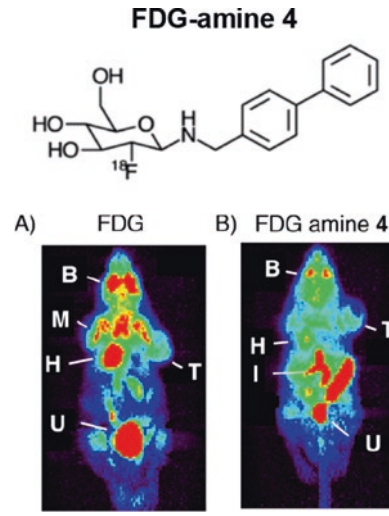

Fig. 15.6 Another approach to imaging pH with PET involves a caged derivative of FDG that selectively degrades to the parent FDG upon exposure to acidic pH. Structure of FDG-amine 4, which at low pH decomposes to FDG (*top*). (**a**) PET imaging with FDG in PC3 prostate tumor-bearing mice (*T* tumor, *B* brain, *M* muscle and brown fat, *H* heart, *U* urinary bladder). The tumor is imaged, as well as typical organs that take up FDG, such as the brain, heart and brown fat. (**b**) PET imaging with the pH sensitive FDG-amine 4 shows primarily tumor uptake, where the acidic microenvironment cleaves at the glycosylamine site, leaving FDG to be taken up by the tumor (from [126])

15.5 Imaging Enzymes in the Tumor Microenvironment

Matrix Metalloproteinases. Matrix metalloproteinases (MMPs) along with other proteases are involved in cellular proteolysis known to be elevated in disease states leading to tumor invasion and metastasis [133, 134]. MMPs are an attractive target for imaging the tumor microenvironment either with activatable probes or MMP inhibitors (MMPIs). There are several good reviews that discuss MMPs as a target for imaging [135, 136]. Another MMP biomarker, membrane type-1 matrix metalloproteinase (MT1-MMP) is a protease that activates MMP-2, which mediates cleavage of extracellular matrix components indicated in tumor progression and metastasis [137–140].

PET/SPECT Agents for imaging MMPs. MMPIs consist of natural and synthetic inhibitors that bind zinc via moieties that include hydroxamate, phosphonate, thiol, carboxylate or barbiturate [135]. A recent paper reported a ^{18}F-labeled hydroxamate-based inhibitor (ML5) for imaging of both MMPs, and disintegrin and metalloproteinase (ADAM) levels in vivo to visualize and quantify overexpression of MMPs and ADAMs [141]. ML5 that was acylated directly with N-succinimidyl-4-[^{18}F]fluorobenzoate showed nanomolar affinity for MMPs and ADAMs, and was brought for PET imaging of HT1080 tumor-bearing mice. The tumor showed modest, but potentially specific, uptake in the tumor. Co-administration of a blocking dose blocked many tissues, including tumor. A cyclic decapeptide (CLP: Cys-Leu-Pro-Gly-His-Trp-Gly-Phe-Pro-Ser-Cys) was studied for its inhibitory selectivity toward MMP-2/9 [142]. The CLP was labeled with ^{99m}Tc with high yield, stable in serum, and accumulated in the uterus, lung, liver and spleen related to MMPs of normal rats, which could contribute to future imaging of metastatic tumors that overexpress MMPs. Another interesting dual imaging probe combined an RGD motif ($\alpha_v\beta_3$ integrin binding), ^{64}Cu-DOTA, PLGVR (MMP-2 cleavage substrate), and ^{123}I-Y for imaging $\alpha_v\beta_3$ integrin positive (M21) and negative (M21L) human melanoma cell localization and pathophysiology [143]. The PET/SPECT imaging probe (c(RGDfE)K(^{64}Cu-DOTA) PLGVR^{123}I-Y) was successfully shown to target $\alpha_v\beta_3$ integrin and detect MMP-2 activity with IC_{50} value in the nanomolar range (83.4 ± 13.2 nM).

There are a few non-inhibitory type imaging probes for MMPs. Specific human MMP-9 (K_d = 20 nM) cleavable RNA aptamers were developed and imaged with ^{99m}Tc for ex vivo imaging of human brain tumors [144]. A truncated aptamer was shown to retain binding affinity and discriminate MMP-9 vs. other human MMPs. MT1-MMP imaging probes consisting of single chain antibody fragments (MT1-scFv) and a dimer (MT1-diabody) were labeled with ^{111}In and imaged in vitro and in vivo [145]. Both probes showed similar tumor accumulation (1–1.5%ID/g) and corresponding MT1-MMP positive areas in ex vivo autoradiography; however, there was extensive uptake in the kidneys (~100%ID/g for the diabody and ~200%ID/g for the scFv), and high liver uptake as well (20–40%ID/g). A study to determine the tumor specificity of ^{177}Lu/^{125}I radiolabeled MMP-2/9 activatable cell-penetrating peptides (ACPPs) was performed on BT-20 (low expression of MMP-9) and s.c. HT1080 (high expression of MMP-9) tumor-bearing mice [146]. The work showed similar uptake in both tumor-bearing mouse model and suggested that probe activation (cleavage) occurs in the vasculature instead of by tumor-specific MMP-9.

Advancement of PET and SPECT imaging probes for the tumor microenvironment are currently being developed, and progress has been made on some innovative probes (discussed above). The results from these studies have provided options and inspiration for future imaging probes and currently utilized radiotracers. Although the nuclear approach in designing imaging probes has advantages of sensitivity and depth, there has been minimal success in the discovery of an MMP-2/9 specific tracer to compete with other imaging modalities (specifically, fluorescence).

Fluorescence Imaging of MMPs. MMP ACPPs are emerging tissue-specific proteases

without nonspecific activation imaging probes for MMP overexpression in tumor microenvironments [147, 148]. Using MMP as a biomarker has been shown to be sensitive enough for optical tomography to determine tumor angiogenesis and invasiveness [149]. Skin squamous cell xenografts were studied and imaged in vivo at different angiogenic and invasive stages using an activatable fluorescence probe [149] (Fig. 15.7). In another study, a nanoprobe system that is activated by MMP-2 was detected by FRET with high efficiency and low toxicity in MMP-2 overexpressed tumors [150].

Protein nanocages have also been used to selectively image MMP-2 activity in metastatic tumors [151] (Fig. 15.8). The nanocages were conjugated to metastatic cancer cell-targeted protein (CTT: CTTHWGFTLC) and imaged in near-IR fluorescence in vitro and in vivo. Gold nanoparticles functionalized with a MMP-2 cleavable peptide (CPLGLAGG) and doxorubicin has been tested in tumor-bearing mice [152]. Tumor growth was inhibited and imaged simultaneous by fluorescence upon MMP cleavage. Imaging of MMP-2/9 was investigated using near-infrared triple-helical peptide conjugated to cypate dyes [153]. In mice bearing human fibrosarcoma xenografted tumors, fluorescence imaging at the tumor site was indicated by cleavage of cypate$_3$-THP. Anti-MT1-MMP monoclonal antibody (MT1-hlC7L) conjugated to micelles with encapsulated NIR dyes were used to image C6 glioma tumor-bearing mice [154]. The probes were specific in detecting MT1-MMP expressing tumors.

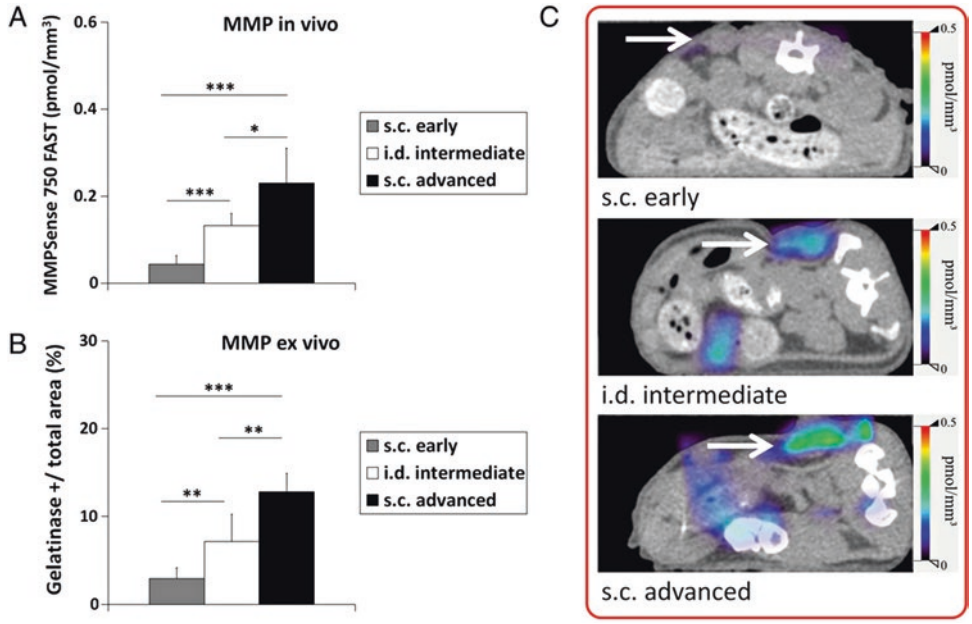

Fig. 15.7 Matrix metalloproteinases can be imaged by activatable fluorescence probes. MMP activity differs significantly between the HaCaT-A-5RT3 tumors at differential angiogenic and invasive stages. (**a**) Assessment of MMP activity in vivo by FMT-μCT imaging reveals significant differences in intratumoral concentrations of activated MMPSense 750 FAST between s.c. advanced (n = 5), i.d. intermediate (n = 5), and s.c. early (n = 7) tumors. Highest concentrations are recorded for s.c. advanced tumors at the highly angiogenic and invasive stage, whereas lowest concentrations are found in s.c. early tumors at the onset of angiogenesis and invasion. (**b**) Quantification of in situ zymography of MMP activity on tumor sections confirms the in vivo data. (**c**) Representative FMT/μCT fusion images of tumor-bearing mice (*transverse plane*) show the fluorescent signals of activated MMPSense 750 FAST in s.c. early, i.d., and s.c. advanced tumors (tumors indicated by a *white arrow*). The additional fluorescent signals found in the intestine region can occur from hepatobiliary excretion of the probe through the intestine [149]

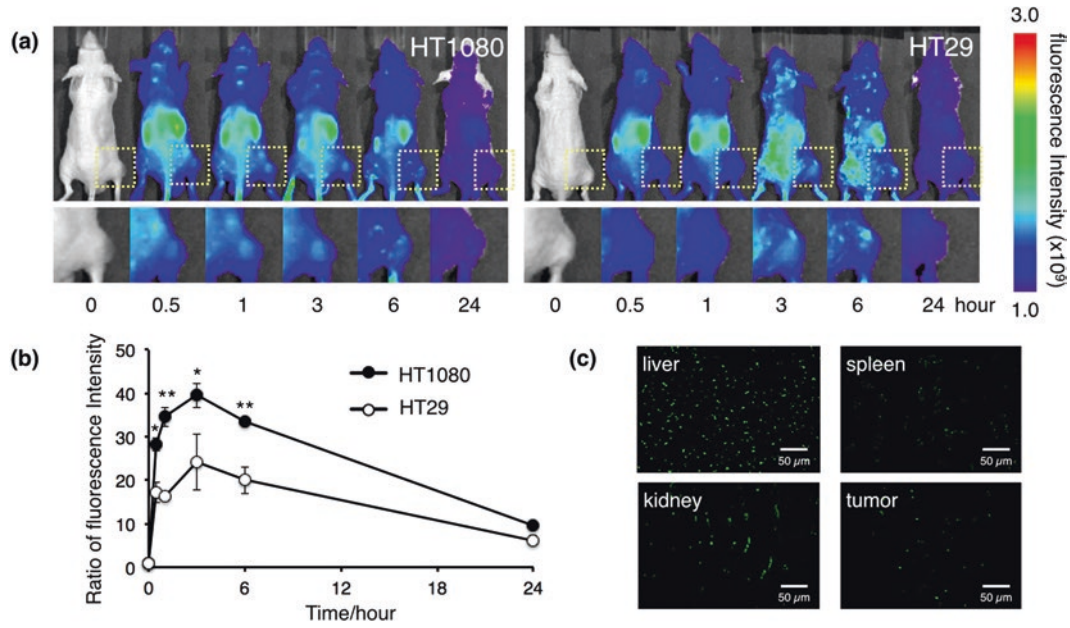

Fig. 15.8 Protein nanocages can selectively image MMP-2 activity in metastatic tumors *in vivo*. (**a**) *In vivo* real-time NIR fluorescence imaging of intravenously injected Alexa Fluor 750-labeled HspG41C-CTT in HT1080 and HT29 tumor-bearing mice. Time-dependent, tumor-targeting specificities of the nanocages were monitored by the IVIS system. Square regions indicate solid tumor growths of subcutaneously injected cancer cells; (**b**) Fluorescence signal intensity ratio of the tumor/background obtained from *in vivo* images. $*p < 0.05$; $**p < 0.01$; (**c**) Organ sections of tumor-bearing mice injected intravenously with Alexa Fluor 488-labeled HspG41C-CTT at 3 h post-injection [151]

Silicon-rhodamine-based near-IR dark quenchers (SiNQs) were shown to quench fluorescence over 780 nm region and detected MMP activity in vitro and in vivo [155]. Improvements on fluorophore pairs used as ACPPs was explored using $Ir(ppy)_3$ and Cy5 for tumor-related MMP-2/9 imaging [156]. In an in vitro evaluation, quenching of the luminophores and shortening of luminescence was reversed upon MMP cleavage. Using a MMP-activatable photoacoustic probe (Alexa750-CXeeeeXPLGLAGrrrrXK-BHQ3) FCT133 thyroid tumors implanted s. c. in nude mice were imaged [157]. Alexa750 fluorescence and photoacoustic imaging showed active forms of MMP-2 and MMP-9 in FTC133 tumor homogenates.

Due to the specificity and efficacy of the fluorescent activatable probes, only a small number of inhibitory type fluorescent probes for MMPs. A Cy5.5-labeled MMP inhibitor (Cy5.5-AF489) was compared to commercially available ACPPs (MMPSenseTM 680 and MMPSenseTM 750 FAST) in xenografted mice [158]. The MMP inhibitor Cy5.5-AF489 showed faster imaging and signal in MMP-active tumors compared to ACPPs.

MRI probes for imaging MMPs. MRI can be used to image MMP biomarkers as well. Iron oxide nanoparticles (IONPs) were designed to undergo cleavage by MMPs resulting in a nanocluster with enhanced T_2 properties [159]. In vitro studies on cells expressing MMP-2/9 and CXCR4 showed T_2 signal enhancements. ACPPs have demonstrated dual targeting for integrin αvβ3 and MMP-2 for imaging and chemotherapy (MMAE: monomethylauristatin) in vivo [160]. Mice treated with cyclic-RGD-PLGC(Me) AG-MMAE-ACPP had improved probe penetration into MDA-MB-231 tumors. Another group has imaged IONPs (ferumoxytol) with a MMP-14 ACPP azademethylcolchicine (ICT) in MMTV-PyMT breast cancer cells in vitro [161].

Theranostic nanoparticles (TNPs) showed proof of concept in tumor specificity, drug delivery and imaging. An interesting activatable ^{19}F-probe was designed to be "off" until cleavage by MMP or nitroreductase (NTR) [162]. Upon cleavage the probe aggregates disassemble turning "on" an imaging signal. Imaging of MMP secreted from tumor cells was shown in vitro, although thus far no in vivo imaging has been reported.

Imaging Cysteine Cathepsins. Cathepsin family of proteases have important roles in normal and diseased cellular physiology [163]. In certain cancers, cysteine cathepsins are upregulated and have been used as cancer biomarkers [164, 165]. The majority of imaging probes using cathepsin activation/cleavage involve near-infrared (NIR) fluorescence agents. There are a handful of PET tracer probes that target cysteine cathepsin as discussed below.

A unique PET tracer probe that inhibits cathepsins was achieved by synthesizing a fluorine-containing azadipeptide nitrile ([^{18}F]**3**) [166]. The azadipeptide nitrile was alkylated with 2-[^{18}F]fluoroethynosylate. In vitro, in vivo, and ex vivo studies were done as well as biodistrubtion and biokinetics in rats, NMRI mice and NMRI nude mice bearing NCI-H292 tumor xenografts. The tracer [^{18}F]**3** showed slow blood clearance, reversible tumor accumulation of the tracer in tumor-bearing mice, confirmed the presence of cathepsins (L, S, K and B) and visualized tumor-associated cathepsins in vivo with tumor:muscle ratios of 10–15, and tumor:blood ratios <1. Another group used a cathepsin inhibitor, acyloxymethyl ketones (AOMKs), with ^{64}Cu-Z-FK(DOTA)-AOMK (^{64}Cu-GB170) as a PET tracer for in vitro and in vivo studies [167]. Small animal PET imaging on MDA-435 and C2C12/Ras tumor-bearing mice with ^{64}Cu-GB170 confirmed in vivo tumor uptake, and selectivity for cysteine cathepsins. SPECT imaging was also employed to optimize cathepsin-targeting polymers to reduce non-target accumulation [168]. N-(2-hydroxypropyl)-methacrylamide (HPMA) copolymers were made with cathepsin S linkers and radiolabeled with ^{177}Lu-DOTA. Normal CF-1 and HPAC tumor-bearing SCID mice were imaged to study structure-activity relationship with the length of the linker group, which was found to be tissue specific in vivo. Poly-L-glutamate (PLG) as a tumor protease activated MRI probe visualized cathepsins in tumors in vivo [169]. Using the CEST effect from amine protons of glutamate moieties generated from cathepsin cleavage of PLG, cathepsins were successfully imaged in rat brain gliosarcoma model in a high resolution (9.4T) MRI.

Cathepsin-activatable fluorescence probes can be divided into peptide and nonpeptide probes, although peptide based probes have been more widely studied. For example, hydroxymethylrhodamine (HMRG)-based fluorescence probes (Z-Phe-Arg-HMRG and Z-Arg-Arg-HMRG) are colorless until they are hydrolyzed by cathepsins resulting in strong fluorescence signal [170]. The probes were visualized in human ovarian cancer cells lines (SHIN-3, SKOV-3, and OVCAR-3) in mouse models in vivo. Another group made an activatable peptide probe on glycol chitosan nanoparticles (280 nm in diam.) specific for cathepsin B cleavage [171]. They were able to discriminate in vivo among three metastatic mouse models (4T1-luc2 liver metastases, RFP-B16F10 lung metastases, HT1080 peritoneal metastases). Other peptide probes based on FRET have also shown selectivity upon cleavage with cathepsin B [172, 173]. Cathepsin-activatable fluorescent probe sensitivity has also been studied comparing tumor and normal muscle in mice models for soft tissue sarcoma before and after radiation therapy [174], and in human cathepsin E positive cells (MPanc96-E) implanted in nude mice [175]. Both studies found significant sensitivity in vivo and in vitro. Certain modifications to probes, such as conjugation of palmitoic acid (lipidation), have resulted in favorable properties to increase the retention of a cathepsin S-specific agent in tumor cells in vivo and in vitro [176]. An interesting non-peptidic, cathepsin, S-directed quenched activity based probe (BMV083) was made and imaged in vivo in a breast cancer model [177]. The agent showed high tumor-specific fluorescence and targeting to M2 phenotypic macrophages.

15.6 Imaging Integrins in the Tumor Microenvironment

Integrins have become effective targets for imaging the tumor microenvironment since the discovery of their role in cell adhesion. There are 24 different types of integrins composed of α and β heterodimeric subunits. Integrin receptors can be classified into four categories based on their ligand binding ability; RGD receptors, collagen receptors, laminin receptors, and leukocyte-specific receptors [178, 179]. Certain integrins such as $\alpha_v\beta_6$ are upregulated in tumors yet are almost undetectable in normal tissue. An overwhelming majority of integrins used in targeting the tumor microenvironment focus on the RGD receptors [180], but other integrin receptors are also being investigated. Using integrins to image the tumor microenvironment has been successful in PET, SPECT, fluorescence and MR imaging. A brief compilation of integrin probes related to imaging the tumor microenvironment are discussed.

PET tracers for imaging integrins. PET tracers coupled to integrin ligands have provided a feasible means of imaging integrins that are upregulated in angiogenesis. Progress has been made using ^{18}F, ^{64}Cu and ^{68}Ga radionuclides. For example, a study evaluating the formulation of an integrin $\alpha_v\beta_3$ imaging probes in U87MG tumor-bearing mice found that ^{18}F-AlF-NOTA-E[PEG$_4$-cRGDfk)]$_2$ had highest tumor uptake and lowest liver accumulation compared to ^{18}F-AlF-NOTA-E[c(RGDfK)]$_2$ and ^{18}F-AlF-NOTA-PEG$_4$-E[c(RGDfK)]$_2$ [181]. Integrins $\alpha_v\beta_3$ and $\alpha_v\beta_5$ were targeted using [^{18}F]fluciclatide, an RGD peptide developed by industry, in 18 patients (melanoma and renal cell carcinoma (RCC)) to compare PET imaging of angiogenesis with integrin expression in tumors [182] (Fig. 15.9). All tumors showed significant [^{18}F]fluciclatide uptake as well as correlation with $\alpha_v\beta_3$ and $\alpha_v\beta_5$ integrins expression in melanoma and RCC tumor tissue (Fig. 15.9). An $\alpha_5\beta_1$ integrin receptor was targeted with [^{18}F]FProp-Cys(*)-Arg-Arg-Glu-Thr-Ala-Trp-Ala-Cys(*)-OH in human melanoma M21 ($\alpha_v\beta_3$-positive and $\alpha_5\beta_1$-negative), human melanoma M21-L ($\alpha_v\beta_3$-negative and $\alpha_5\beta_1$-negative), and human prostate carcinoma DU145 ($\alpha_v\beta_3$-negative and $\alpha_5\beta_1$-positive) cells to study receptor-specific binding [183]. Blocking studies with mice bearing $\alpha_5\beta_1$-negative M21 tumors gave conflicting results compared to the in vitro studies, which showed high affinity for $\alpha_5\beta_1$ integrin, warranting further investigations. Integrin $\alpha_v\beta_3$ receptor was also targeted using ^{18}F-E[c(RGDfK)$_2$] in healthy KM mice and U87MG tumor-bearing mice to study the biodistribution of the PET tracer [184]. It was found to target tumors with high uptake (5.2 ± 0.56%ID/g) 1 h post injection. Other peptide ligands like cysteine knot peptides, R_o1 and S_o2, which have 3–6 nM affinity for integrin $\alpha_v\beta_6$, have been radiolabeled with ^{18}F-fluorobenzoate for PET imaging of BxPC3 pancreatic adenocarcinoma xenografts on mice [185]. The radiolabeled peptides, ^{18}F-fluorobenzoate-R_o1 and ^{18}F-benzoate-S_o2, showed 2.3 ± 0.6 and 1.3 ± 0.4%ID/g, respectively in BxPC3 xenografted tumors at 0.5 h post injection. Another well-known $\alpha_v\beta_3$ integrin PET probe is [^{18}F]Galacto-RGD, which has been shown to image high-grade human carotid plaques in patients correlating well with ex vivo autoradiography of surgical specimens [186]. An $\alpha_6\beta_1$ integrin PET probe was developed using a peptide-porphyrin azide-alkyne conjugation [187]. The probe was radiolabeled with ^{68}Ga and found have higher activity in HeLa cells with higher $\alpha_6\beta_1$ integrin expression compared to the U87 cells which display minimal integrin expression.

Several synthetic strategies have emerged to incorporate radionuclides more efficiently to integrin ligands for imaging upregulated integrins in the tumor microenvironment. One methods involves coordinating aluminum [^{18}F]fluoride into NOTA chelators [188, 189]. An $\alpha_v\beta_6$ integrin targeted peptide (A20FMDV2) was evaluated as a radiotracer (Al[^{18}F]-NOTA-PEG$_{28}$-A20FMDV2) in vitro and in vivo in $\alpha_v\beta_6$(+) and $\alpha_v\beta_6$(−) cells and xenograft mice, respectively [190]. The Al[^{18}F]-NOTA radiolabeling was found to be efficient, and the tracer showed $\alpha_v\beta_6$ selectivity in vitro and in vivo, although kidney uptake was significant even after 4 h post

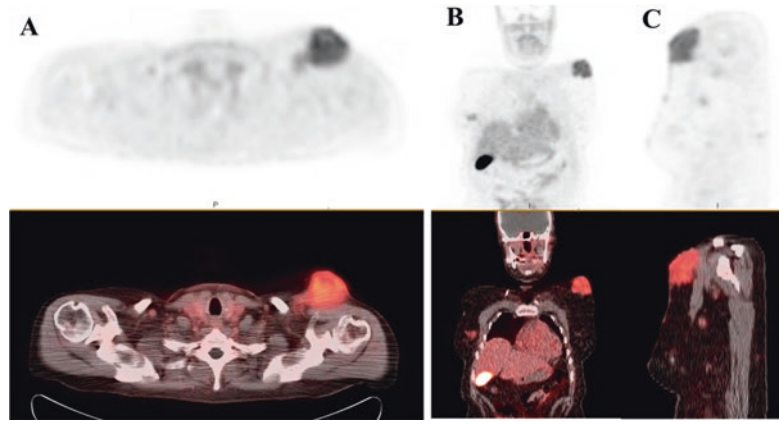

Fig. 15.9 Integrins $\alpha_v\beta_3$ and $\alpha_v\beta_5$ were imaged with [^{18}F] fluciclatide, an RGD peptide, in 18 patients (melanoma and renal cell carcinoma (RCC)) to compare PET imaging of angiogenesis with tumor integrin expression. [^{18}F] Fluciclatide PET/CT axial (**a**) sagittal (**b**) and coronal (**c**) images in patient four (malignant melanoma) show focal radiotracer uptake within a left supraclavicular mass, with SUV80% max 6.5, as well as in other soft tissue nodules [182]

injection. Another integrin probe, 2-[^{18}F]fluoroethyl triazolyl conjugated c(RGDyK) peptide, was designed using Cu(I)-catalyzed conjugation showing good stability in vivo (U87MG tumors) and tumor-to-background ratio of 1.6 ± 0.3%ID/g 1.5 h post injection [191].

Copper-64 is an attractive radioisotope for PET integrin probes to image the tumor microenvironment. Integrin $\alpha_v\beta_6$ has been targeted by several groups with various ^{64}Cu PET probes as a biomarker for several cancers such as non-small cell lung cancer (NSCLC). One groups developed a divalent probe, ^{64}CuAcD10, with low kidney accumulation and good tumor uptake in mice with either H2009 or H460 xenografts (Ajay N [192].). Another study evaluated chelators (CB-TE1A1P, DOTA, NOTA and BaBaSar) for ^{64}Cu by radiolabeling an $\alpha_v\beta_6$ integrin targeting peptide, A20FMDV2, respectively [193]. The findings suggest that the best chelator depended on the stability, selectivity or pharmacokinetics desired out of the PET probe (Fig. 15.10). Other ^{64}Cu chelates have been used to image known upregulated integrins in the tumor microenvironment such as $\alpha_4\beta_1$ and $\alpha_v\beta_3$. ^{64}Cu-(CB-TE2A)-LLP2A was investigated for imaging bone marrow derived cells involved in bone metastasis in nude mice injected with MDA-MB-231/firefly luciferase human breast tumor cells (VL4–4-negative) [194]. Higher uptake in bone corresponded with mice that eventually had bone metastases, and this was confirmed by flow cytometry for the presence of hematopoietic progenitor cells. Dually radiolabeled peptides for imaging and targeting $\alpha_v\beta_3$ integrin have been developed containing an RGD sequence for binding $\alpha_v\beta_3$ integrin, DOTA for radiolabeling with ^{64}Cu, PLGVRY for MMP2 cleavage, and terminal tyrosine labeled with ^{125}I (c(RGDfE)K(DOTA)PLGVRY) [143]. The dually radiolabeled probe showed high affinity of $\alpha_v\beta_3$ integrin in substrate competition and cell binding assays.

SPECT agents for imaging integrins. Several SPECT probes have been explored to target integrins for imaging the tumor microenvironment using ^{99m}Tc, ^{125}I, and ^{111}In. An $\alpha_v\beta_3$ and $\alpha_v\beta_5$ integrin SPECT imaging probe was developed to evaluate its dosimetry in seven healthy and three breast cancer patients and in mice with MCF7 tumors [195]. The RGD peptide was coupled to ethylenediamine-N,N′-diacetic (EDDA) which favors renal excretion with ^{99m}Tc-labeled hydrazinonicotinamide (HYNIC). The probe, ^{99m}Tc-EDDA/HYNIC-E-[c(RGDfK)]$_2$ showed high tumor uptake in patients with malignant lesions and rapid bowel clearance. A ^{99m}Tc-labeled cRGD was used to monitor hepatic stellate cells (HSC) which express $\alpha_v\beta_3$ integrins in fibrotic rat

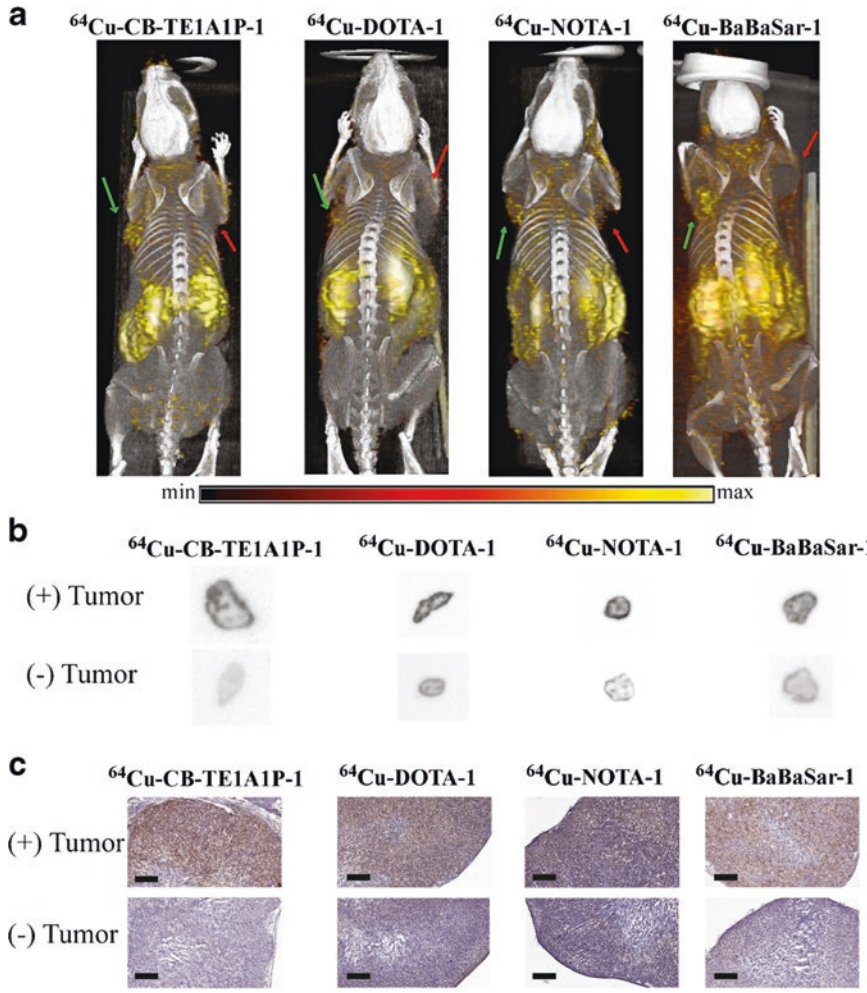

Fig. 15.10 PET imaging of $\alpha_v\beta_6$ integrin with a ^{64}Cu-labeled peptide (A20FMDV2) conjugated with CB-TE1A1P, DOTA, NOTA and BaBaSar chelators was performed to determine the best chelator for optimal tumor uptake and normal tissue biodistribution. (**a**) Reconstructed 3D PET/CT images showing (+) (*green arrow*) and (−) (*red arrow*) tumors. Mice were anesthetized using 2–3 % isoflurane and received 150–250 μCi of formulated radiotracer via tail vein. All images were acquired 4 h p.i. using 20 min static scans. (**b**) Autoradiography slices (20 μm) of (+) and (−) tumors, sectioned at 4 h p.i. and exposed overnight. Each slice read at a 50-μm resolution. (**c**) Histology slices (5 μm) from (+) and (−) tumors after immunohistochemistry staining for αvβ6 viewed at ×4 magnification. Scale bar = 400 μm [193]

livers [196]. The study found the tracer to distinguish the different stages of liver fibrosis in rats. Other SPECT probes for imaging the tumor microenvironment also target $\alpha_v\beta_6$ integrins. One such probe (^{99m}Tc-HHK) was studied in BxPC-3 (integrin $\alpha_v\beta_6$-positive) and HEK293 (integrin $\alpha_v\beta_6$-negative) in vitro and in vivo [197]. The study found ^{99m}Tc-HHK showed high specificity for integrin $\alpha_v\beta_6$, with highest uptake at 0.5 h post injection. An $\alpha_v\beta_6$ integrin targeting cysteine knot peptide, S_o2, coupled to a single amino acid chelate (SAAC) to give ^{99m}Tc-SAAC-S_o2 and evaluated in vitro and in vivo studies [198]. In vitro studies compared HCC4009 and BxPC-3 cell lines (integrin $\alpha_v\beta_6$-positive) and H838 and 293 T cell lines (integrin $\alpha_v\beta_6$-negative) to find significant uptake in integrin $\alpha_v\beta_6$-positive cells. In vivo studies in nude mice bearing HCC4009 and H838

tumor xenografts showed uptake in antigen positive tumors and high tumor-to-background ratios (6.81 ± 2.32%ID/g) at 6 h post injection.

Probes for $\alpha_v\beta_6$ integrin targeting were designed to image pancreatic ductal adenocarcinoma (PDAC) were examined in a biodistribution assay, in vivo blocking study and SPECT imaging of tumor-bearing mice [199]. The study found one of four probes (^{125}I-HFMDV2) showed the highest affinity for $\alpha_v\beta_6$ integrin in AsPC-1 cells and 3–5 times greater uptake in AsPC-1 xenografts compared to MIA PaCA-cells and xenografts. Another study developed an indium-111-labeled tetra[DTPA]-A20FMDV2 to investigate the development of fibrosis in a murine model (bleomycin-induced lung injury) by monitoring lung hydroxyproline, $\alpha_v\beta_6$ integrin, and *itgb6* messenger RNA [200]. The SPECT probe enabled quantifiable detection in lungs 1 h post injection compared to several controls.

Fluorescent probes for imaging integrins. Optical imaging with various near-infrared (NIR) fluorescence probes has been successful in imaging the tumor microenvironment. One study targeted $\alpha_v\beta_6$ integrin binding peptide (HK) with a NIR phthalocyanine dye (Dye-SA-B-HK) to image subcutaneous and orthotopic BxPC-3 cancer xenografts in mice for optical image-guided surgery and phototherapy [201] (Fig. 15.11) and found impressive antitumor effects both in vitro and in vivo. Other targeting agents have included activatable cell-penetrating peptides (ACPP) in combination with integrin targeting coupled to Cy5 dye to achieve improved specificity and sensitivity in imaging MDA-MB-231 tumor-bearing mice [160]. This study also showed the dual targeting probe combined with a chemotherapeutic (monomethylauristatin, MMAE), finding improved efficacy in MDA-MB-231 orthotopic human and syngeneic Py230 murine breast tumors. Gold nanostars (Au NS) were explored as a platform for targeting integrin with cyclic RGD and fluorescent probe (MPA) or anti-cancer drug (DOX) [152]. The study demonstrated the photo-thermal therapy and chemotherapy in MDA-MB-231 cell lines and in S180 tumor-bearing mice. Imaging intracranial medulloblastoma has also been investigated using $\alpha_5\beta_1$ integrin-binding cysteine knot peptide (EETI 2.5F and EETI 2.5F-Fc) conjugated to a fluorescent dye (AF680) in tumor-bearing mice [202]. The optical imaging probes were found to be to cross the blood-brain-barrier to the tumor showing impressive brain tumor imaging compared to other cysteine knot peptides conjugated to c(RGDfK). A fluorescent imaging probe (tetraphenylsilole, TPS) coupled to two integrin-targeting peptide (cRGD) uses aggregation induced emission (AIE) to image the tumor microenvironment in vitro [203]. Quantitative detection was achieved using the imaging probe (TPS-2cRGD) in MCF-7 and HT29 cancer cells, targeting $\alpha_v\beta_3$-integrin. Another study tested a small peptidomimetic $\alpha_v\beta_3$ integrin antagonist coupled to NIR dye (IntegriSense) for binding specificity in vitro and in vivo [204]. The integrin NIR fluorescent agent exhibited selectivity toward $\alpha_v\beta_3$ and $\alpha_v\beta_5$ integrin in vitro and provided real-time quantification in tumors in vivo. In addition to fluorescence imaging, Cerenkov luminescence imaging (CLI) has also been shown in male athymic mice with DX3puroβ6 ($\alpha_v\beta_6$-positive) and DX3puro ($\alpha_v\beta_6$-negative) tumors [205]. CLI agents, ^{90}Y-DOTA-PEG$_{28}$-A20FMDV2 and ^{90}Y-DOTA-Ahx-A20FMDV2 were investigated showing good correlation between CLI quantification and biodistribution, but also having low uptake in $\alpha_v\beta_6$-positive tumors.

MR agents for imaging integrins. MR imaging has more recently been employed to image integrins in the tumor microenvironment. Superparamagnetic iron oxide (SPIO)-loaded cRGD PEGylated polyion complex vesicles (PICsomes) targeting $\alpha_v\beta_3$ and $\alpha_v\beta_5$ integrins have recently been investigated to image the neovasculature in an orthotopic glioblastoma model [206]. The 40% PEG on distal end of the PICsomes to cRGD moieties was found to accumulate in tumor neovasculature after 24 h, and were able to identify tumor lesions using T_2-weighted MRI. Other forms of nanoparticles like magnetoliposomes have been studied to also target integrins [207]. The study evaluated tumor angiogenesis targeting of anti- $\alpha_v\beta_3$ antibody guided 3-step pretargeting approach using modi-

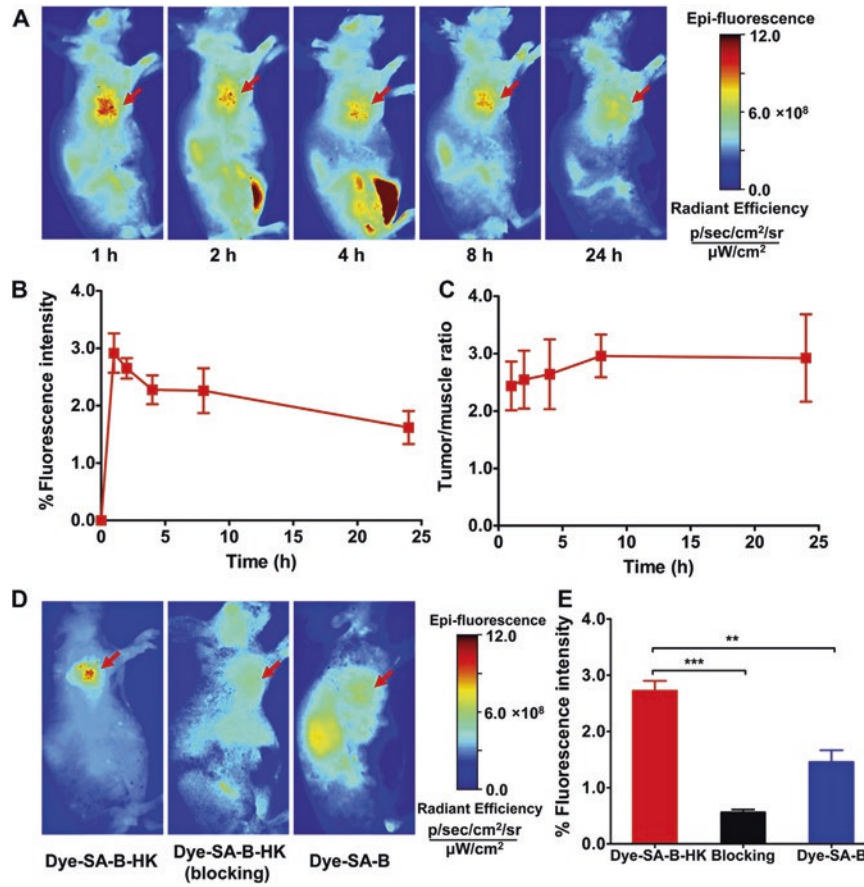

Fig. 15.11 Optical imaging in combination with photodynamic therapy has been performed in a mouse model of pancreatic cancer with near-infrared phthalocyanine dye (Dye-SA-B) conjugated to an $\alpha_v\beta_6$ integrin targeted peptide (HK). (**a**) Representative near-infrared fluorescence sagittal images of Dye-SA-B-HK in BxPC-3 tumor-bearing nude mice at 1, 2, 4, 8, and 24 h postinjection. (BeC) Quantified in vivo tumor uptake (**b**) and tumor-to-muscle ratios (**c**) of Dye-SA-B-HK in BxPC-3 tumor-bearing nude mice. Results are expressed as mean ± SD (n ¼ 5). (DeE) In vivo nearinfrared fluorescence sagittal imaging (**d**) and quantified tumor uptake (E) of BxPC-3 tumor-bearing nude mice at 2 h after intravenous injection of Dye-SA-B-HK (with or without the blocking of an excess dose of the HK peptide) or Dye-SA-B. Results are expressed as mean ± SD (n 1/4 5 per group). **P < 0.01, ***P < 0.001. *Arrows* indicate the tumors in all cases [201]

fied SPIO in liposomes. The magnetoliposomes showed greater signal enhancement in tumor area (7.0%) by T_2-weighted MR images compared to the control (2.0%).

15.7 Conclusions

There are many aspects of the tumor microenvironment and having a way to non-invasively monitor changes of both cell types and physiological parameters of the extracellular milieu is of great importance, both in humans and in small animal models of cancer. The literature reviewed highlights numerous pathways and strategies for imaging not just the growth of tumors, but the changes in the microenvironment over time and after treatment. Some of these are already being investigated in humans. Additionally, there is a wealth of research on investigating novel approaches in small animal models of cancer, both for gathering mechanistic information non-invasively over time, as well as for translation of imaging strategies to humans.

Acknowledgements The authors would like to acknowledge funding from the National Cancer Institute (R01 CA214018 (CJA) and R21 EB023364 (WBE)), University of Pittsburgh Physicians (UPP) Academic Foundation Award (WBE) and Department of Energy and National Institute of Biomedical Imaging and Bioengineering (DE-SC0008833; for MCZA).

References

1. Hanahan D, Weinberg RA. Hallmarks of cancer: the next generation. Cell. 2011;144:646–74.
2. Huang T, Civelek AC, Li J, Jiang H, Ng CK, Postel GC, Shen B, Li XF. Tumor microenvironment-dependent 18F-FDG, 18F-fluorothymidine, and 18F-misonidazole uptake: a pilot study in mouse models of human non-small cell lung cancer. J Nucl Med. 2012;53(8):1262.
3. Yanar M, Abel F, Haalck T, Klutmann S, Schumacher U. The microenvironment in the human lung partly determines the site of the first metastasis. Anticancer Res. 2014;34:3845–9.
4. Elinav E, Nowarski R, Thaiss CA, Hu B, Jin C, Flavell RA. Inflammation-induced cancer: crosstalk between tumours, immune cells and microorganisms. Nat Rev Cancer. 2013;13:759–71.
5. Dvorak HF. Tumors: wounds that do not heal. Similarities between tumor stroma generation and wound healing. N Engl J Med. 1986;315:1650–9.
6. Pages F, Galon J, Dieu-Nosjean MC, Tartour E, Sautes-Fridman C, Fridman WH. Immune infiltration in human tumors: a prognostic factor that should not be ignored. Oncogene. 2010;29:1093–102.
7. Rashidian M, Keliher EJ, Bilate AM, Duarte JN, Wojtkiewicz GR, Jacobsen JT, Cragnolini J, Swee LK, Victora GD, Weissleder R, Ploegh HL. Noninvasive imaging of immune responses. Proc Natl Acad Sci U S A. 2015;112:6146–51.
8. Forssell J, Oberg A, Henriksson ML, Stenling R, Jung A, Palmqvist R. High macrophage infiltration along the tumor front correlates with improved survival in colon cancer. Clin Cancer Res. 2007;13:1472–9.
9. Denardo DG, Andreu P, Coussens LM. Interactions between lymphocytes and myeloid cells regulate pro- versus anti-tumor immunity. Cancer Metastasis Rev. 2010;29:309–16.
10. Grivennikov SI, Greten FR, Karin M. Immunity, inflammation, and cancer. Cell. 2010;140:883–99.
11. Qian BZ, Pollard JW. Macrophage diversity enhances tumor progression and metastasis. Cell. 2010;141:39–51.
12. Sica A, Bronte V. Altered macrophage differentiation and immune dysfunction in tumor development. J Clin Invest. 2007;117:1155–66.
13. Wang Y-C, He F, Feng F, Liu X-W, Dong G-Y, Qin H-Y, Hu X-B, Zheng M-H, Liang L, Feng L, Liang Y-M, Han H. Notch signaling determines the M1 versus M2 polarization of macrophages in antitumor immune responses. Cancer Res. 2010;70:4840–9.
14. Galdiero MR, Garlanda C, Jaillon S, Marone G, Mantovani A. Tumor associated macrophages and neutrophils in tumor progression. J Cell Physiol. 2013;228:1404–12.
15. Chen J, Yao Y, Gong C, Yu F, Su S, Chen J, Liu B, Deng H, Wang F, Lin L. CCL18 from tumor-associated macrophages promotes breast cancer metastasis via PITPNM3. Cancer Cell. 2011;19:541–55.
16. Sica A, Mantovani A. Macrophage plasticity and polarization: in vivo veritas. J Clin Invest. 2012;122:787–95.
17. Pérez-Medina C, Tang J, Abdel-Atti D, Hogstad B, Merad M, Fisher EA, Fayad ZA, Lewis JS, Mulder WJM, Reiner T. PET imaging of tumor-associated macrophages with 89Zr-Labeled high-density lipoprotein nanoparticles. J Nucl Med. 2015;56:1272–7.
18. Locke LW, Mayo MW, Yoo AD, Williams MB, Berr SS. PET imaging of tumor associated macrophages using mannose coated 64Cu liposomes. Biomaterials. 2012;33:7785–93.
19. Movahedi K, Schoonooghe S, Laoui D, Houbracken I, Waelput W, Breckpot K, Bouwens L, Lahoutte T, de Baetselier P, Raes G. Nanobody-based targeting of the macrophage mannose receptor for effective in vivo imaging of tumor-associated macrophages. Cancer Res. 2012;72:4165–77.
20. Tavare R, McCracken MN, Zettlitz KA, Knowles SM, Salazar FB, Olafsen T, Witte ON, Wu AM. Engineered antibody fragments for immuno-PET imaging of endogenous CD8+ T cells in vivo. Proc Natl Acad Sci U S A. 2014;111:1108–13.
21. Harris AL. Hypoxia—a key regulatory factor in tumour growth. Nat Rev Cancer. 2002;2:38–47.
22. Murdoch C, Muthana M, Lewis CE. Hypoxia regulates macrophage functions in inflammation. J Immunol. 2005;175:6257–63.
23. Semenza GL. Angiogenesis ischemic and neoplastic disorders. Annu Rev Med. 2003;54:17–28.
24. Lee C-T, Boss M-K, Dewhirst MW. Imaging tumor hypoxia to advance radiation oncology. Antioxid Redox Signal. 2014;21:313–37.
25. Vaupel P, Mayer A. Hypoxia in tumors: pathogenesis-related classification, characterization of hypoxia subtypes, and associated biological and clinical implications. Adv Exp Med Biol. 2014;812:19–24.
26. Hsieh CH, Chang HT, Shen WC, Shyu WC, Liu RS. Imaging the impact of Nox4 in cycling hypoxia-mediated U87 glioblastoma invasion and infiltration. Mol Imaging Biol. 2012;14:489–99.
27. Avni R, Cohen B, Neeman M. Hypoxic stress and cancer: imaging the axis of evil in tumor metastasis. NMR Biomed. 2011;24:569–81.
28. Horsman MR, Mortensen LS, Petersen JB, Busk M, Overgaard J. Imaging hypoxia to improve radiotherapy outcome. Nat Rev Clin Oncol. 2012;9:674–87.

29. Mendichovszky I, Jackson A. Imaging hypoxia in gliomas. Br J Radiol. 2014;84(2):S145–58.
30. Sun X, Niu G, Chan N, Shen B, Chen X. Tumor hypoxia imaging. Mol Imaging Biol. 2011;13:399–410.
31. Wang L, Li C. Fluorescence nanoprobe imaging tumor by sensing the acidic microenvironment. Boca Raton: Science Publishers; 2012.
32. Carlin S, Humm JL. PET of hypoxia: current and future perspectives. J Nucl Med. 2012;53:1171–4.
33. Carlin S, Zhang H, Reese M, Ramos NN, Chen Q, Ricketts S-A. A comparison of the imaging characteristics and microregional distribution of 4 hypoxia PET tracers. J Nucl Med. 2014;55:515–21.
34. Hoigebazar L, Jeong JM. Hypoxia imaging agents labeled with positron emitters. Recent Results Cancer Res. 2013;194:285–99.
35. Kelada OJ, Carlson DJ. Molecular imaging of tumor hypoxia with positron emission tomography. Radiat Res. 2014;181:335–49.
36. Kersemans V, Cornelissen B, Hueting R, Tredwell M, Hussien K, Allen PD, Falzone N, Hill SA, Dilworth JR, Gouverneur V. Hypoxia imaging using PET and SPECT: the effects of anesthetic and carrier gas on [64 Cu]-ATSM,[99m Tc]-HL91 and [18 F]-FMISO tumor hypoxia accumulation. PLoS One. 2011;6:e25911.
37. Kurihara H, Honda N, Kono Y, Arai Y. Radiolabelled agents for PET imaging of tumor hypoxia. Curr Med Chem. 2012;19:3282–9.
38. Yip C, Blower PJ, Goh V, Landau DB, Cook GJ. Molecular imaging of hypoxia in non-small-cell lung cancer. Eur J Nucl Med Mol Imaging. 2015;42:956–76.
39. Bell C, Dowson N, Fay M, Thomas P, Puttick S, Gal Y, Rose S. Hypoxia imaging in gliomas with 18F-fluoromisonidazole PET: toward clinical translation. Semin Nucl Med. 2015;45:136–50.
40. Rajendran JG, Krohn KA. F-18 fluoromisonidazole for imaging tumor hypoxia: imaging the microenvironment for personalized cancer therapy. Semin Nucl Med. 2015;45:151–62.
41. Kobayashi K, Hirata K, Yamaguchi S, Kobayashi H, Terasaka S, Manabe O, Shiga T, Magota K, Kuge Y, Tamaki N. FMISO PET at 4 hours showed a better lesion-to-background ratio uptake than 2 hours in brain tumors. J Nucl Med. 2015;56:373.
42. Kawai N, Lin W, Cao W-D, Ogawa D, Miyake K, Haba R, Maeda Y, Yamamoto Y, Nishiyama Y, Tamiya T. Correlation between 18F-fluoromisonidazole PET and expression of HIF-1α and VEGF in newly diagnosed and recurrent malignant gliomas. Eur J Nucl Med Mol Imaging. 2014;41:1870–8.
43. Huang T, Civelek AC, Zheng H, Ng CK, Duan X, Li J, Postel GC, Shen B, Li X-F. 18F-misonidazole PET imaging of hypoxia in micrometastases and macroscopic xenografts of human non-small cell lung cancer: a correlation with autoradiography and histological findings. Am J Nucl Med Mol Imaging. 2013;3:142.
44. Trinkaus ME, Blum R, Rischin D, Callahan J, Bressel M, Segard T, Roselt P, Eu P, Binns D, Macmanus MP. Imaging of hypoxia with 18F-FAZA PET in patients with locally advanced non-small cell lung cancer treated with definitive chemoradiotherapy. J Med Imaging Radiat Oncol. 2013;57:475–81.
45. Zegers CM, van Elmpt W, Wierts R, Reymen B, Sharifi H, Öllers MC, Hoebers F, Troost EG, Wanders R, van Baardwijk A. Hypoxia imaging with [18 F] HX4 PET in NSCLC patients: defining optimal imaging parameters. Radiother Oncol. 2013;109:58–64.
46. Busk M, Mortensen LS, Nordsmark M, Overgaard J, Jakobsen S, Hansen K, Theil J, Kallehauge J, D'Andrea F, Steiniche T. PET hypoxia imaging with FAZA: reproducibility at baseline and during fractionated radiotherapy in tumour-bearing mice. Eur J Nucl Med Mol Imaging. 2013;40:186–97.
47. Peeters SG, Zegers CM, Lieuwes NG, van Elmpt W, Eriksson J, van Dongen GA, Dubois L, Lambin P. A comparative study of the hypoxia PET tracers [18 F] HX4,[18 F] FAZA, and [18 F] FMISO in a preclinical tumor model. Int J Radiat Oncol Biol Phys. 2015;91:351–9.
48. Segard T, Robins PD, Yusoff IF, Ee H, Morandeau L, Campbell EM, Francis RJ. Detection of hypoxia with 18F-fluoromisonidazole (18F-FMISO) PET/CT in suspected or proven pancreatic cancer. Clin Nucl Med. 2013;38:1–6.
49. Chen L, Zhang Z, Kolb HC, Walsh JC, Zhang J, Guan Y. 18F-HX4 hypoxia imaging with PET/CT in head and neck cancer: a comparison with 18F-FMISO. Nucl Med Commun. 2012;33:1096–102.
50. Hu M, Xing L, Mu D, Yang W, Yang G, Kong L, Yu J. Hypoxia imaging with 18F-Fluoroerythronitroimidazole integrated PET/CT and immunohistochemical studies in non–small cell lung cancer. Clin Nucl Med. 2013;38:591–6.
51. Yue J, Yang Y, Cabrera A, Sun X, Zhao S, Xie P, Zheng J, Ma L, Fu Z, Yu J. Measuring tumor hypoxia with 18F-FETNIM PET in esophageal squamous cell carcinoma: a pilot clinical study. Dis Esophagus. 2012;25:54–61.
52. Laurens E, Yeoh SD, Rigopoulos A, Cao D, Cartwright GA, O'Keefe GJ, Tochon-Danguy HJ, White JM, Scott AM, Ackermann U. Radiolabelling and evaluation of novel haloethylsulfoxides as PET imaging agents for tumor hypoxia. Nucl Med Biol. 2012;39:871–82.
53. Servagi-Vernat S, Differding S, Hanin F-X, Labar D, Bol A, Lee JA, Grégoire V. A prospective clinical study of 18 F-FAZA PET-CT hypoxia imaging in head and neck squamous cell carcinoma before and during radiation therapy. Eur J Nucl Med Mol Imaging. 2014;41:1544–52.

54. Murakami M, Zhao S, Zhao Y, Chowdhury NF, Yu W, Nishijima K-I, Takiguchi M, Tamaki N, Kuge Y. Evaluation of changes in the tumor microenvironment after sorafenib therapy by sequential histology and 18F-fluoromisonidazole hypoxia imaging in renal cell carcinoma. Int J Oncol. 2012;41:1593–600.
55. Tachibana I, Nishimura Y, Shibata T, Kanamori S, Nakamatsu K, Koike R, Nishikawa T, Ishikawa K, Tamura M, Hosono M. A prospective clinical trial of tumor hypoxia imaging with 18F-fluoromisonidazole positron emission tomography and computed tomography (F-MISO PET/CT) before and during radiation therapy. J Radiat Res. 2013;54:1078–84.
56. Zips D, Zöphel K, Abolmaali N, Perrin R, Abramyuk A, Haase R, Appold S, Steinbach J, Kotzerke J, Baumann M. Exploratory prospective trial of hypoxia-specific PET imaging during radiochemotherapy in patients with locally advanced head-and-neck cancer. Radiother Oncol. 2012;105:21–8.
57. Sakr T, Essa B, El-Essawy F, El-Mohty A. Synthesis and biodistribution of 99m Tc-PyDA as a potential marker for tumor hypoxia imaging. Radiochemistry. 2014;56:76–80.
58. Giglio J, Fernández S, Pietzsch H-J, Dematteis S, Moreno M, Pacheco JP, Cerecetto H, Rey A. Synthesis, in vitro and in vivo characterization of novel 99m Tc-‘4+ 1’-labeled 5-nitroimidazole derivatives as potential agents for imaging hypoxia. Nucl Med Biol. 2012;39:679–86.
59. Sakr T, Motaleb M, Ibrahim I. 99mTc–meropenem as a potential SPECT imaging probe for tumor hypoxia. J Radioanal Nucl Chem. 2012;292:705–10.
60. Kimura S, Umeda IO, Moriyama N, Fujii H. Synthesis and evaluation of a novel 99m Tc-labeled bioreductive probe for tumor hypoxia imaging. Bioorg Med Chem Lett. 2011;21:7359–62.
61. Tateishi K, Tateishi U, Sato M, Yamanaka S, Kanno H, Murata H, Inoue T, Kawahara N. Application of 62Cu-diacetyl-bis (N4-methylthiosemicarbazone) PET imaging to predict highly malignant tumor grades and hypoxia-inducible factor-1α expression in patients with glioma. Am J Neuroradiol. 2013;34:92–9.
62. Hansen AE, Kristensen AT, Jørgensen JT, McEvoy FJ, Busk M, Van der Kogel AJ, Bussink J, Engelholm SA, Kjær A. 64Cu-ATSM and 18FDG PET uptake and 64Cu-ATSM autoradiography in spontaneous canine tumors: comparison with pimonidazole hypoxia immunohistochemistry. Radiat Oncol. 2012;7:89.
63. Hansen AE, Kristensen AT, Law I, McEvoy FJ, Kjær A, Engelholm SA. Multimodality functional imaging of spontaneous canine tumors using 64 Cu-ATSM and 18 FDG PET/CT and dynamic contrast enhanced perfusion CT. Radiother Oncol. 2012;102:424–8.
64. Bourgeois M, Rajerison H, Guerard F, Mougin-Degraef M, Barbet J, Michel N, Cherel M, Faivre-Chauvet A. Contribution of [64Cu]-ATSM PET in molecular imaging of tumour hypoxia compared to classical [18F]-MISO—a selected review. Nucl Med Rev Cent East Eur. 2011;14:90–5.
65. Bonnitcha PD, Bayly SR, Theobald MB, Betts HM, Lewis JS, Dilworth JR. Nitroimidazole conjugates of bis (thiosemicarbazonato) 64 Cu (II)–potential combination agents for the PET imaging of hypoxia. J Inorg Biochem. 2010;104:126–35.
66. Grigsby PW, Malyapa RS, Higashikubo R, Schwarz JK, Welch MJ, Huettner PC, Dehdashti F. Comparison of molecular markers of hypoxia and imaging with (60)Cu-ATSM in cancer of the uterine cervix. Mol Imaging Biol. 2007;9:278–83.
67. Wu Y, Hao G, Ramezani S, Saha D, Zhao D, Sun X, Sherry AD. [68 Ga]-HP-DO3A-nitroimidazole: a promising agent for PET detection of tumor hypoxia. Contrast Media Mol Imaging. 2015;10(6):465–72.
68. Sano K, Okada M, Hisada H, Shimokawa K, Saji H, Maeda M, Mukai T. In vivo evaluation of a radiogallium-labeled bifunctional radiopharmaceutical, Ga-DOTA-MN2, for hypoxic tumor imaging. Biol Pharm Bull. 2013;36:602–8.
69. Hoigebazar L, Jeong JM, Hong MK, Kim YJ, Lee JY, Shetty D, Lee Y-S, Lee DS, Chung J-K, Lee MC. Synthesis of 68 Ga-labeled DOTA-nitroimidazole derivatives and their feasibilities as hypoxia imaging PET tracers. Bioorg Med Chem. 2011;19:2176–81.
70. Gulaka PK, Rojas-Quijano F, Kovacs Z, Mason RP, Sherry AD, Kodibagkar VD. GdDO3NI, a nitroimidazole-based T 1 MRI contrast agent for imaging tumor hypoxia in vivo. J Biol Inorg Chem. 2014;19:271–9.
71. Pacheco-Torres J, López-Larrubia P, Ballesteros P, Cerdán S. Imaging tumor hypoxia by magnetic resonance methods. NMR Biomed. 2011;24:1–16.
72. Egeland TA, Gulliksrud K, Gaustad JV, Mathiesen B, Rofstad EK. Dynamic contrast-enhanced-MRI of tumor hypoxia. Magn Reson Med. 2012;67:519–30.
73. Gulliksrud K, Øvrebø KM, Mathiesen B, Rofstad EK. Differentiation between hypoxic and non-hypoxic experimental tumors by dynamic contrast-enhanced magnetic resonance imaging. Radiother Oncol. 2011;98:360–4.
74. Stoyanova R, Huang K, Sandler K, Cho H, Carlin S, Zanzonico PB, Koutcher JA, Ackerstaff E. Mapping tumor hypoxia in vivo using pattern recognition of dynamic contrast-enhanced MRI data. Transl Oncol. 2012;5:437–IN2.
75. Wu Y, Zhang W, Li J, Zhang Y. Optical imaging of tumor microenvironment. Am. J. Nucl Med Mol Imaging. 2013;3:1–15.
76. Zheng X, Wang X, Mao H, Wu W, Liu B, Jiang X. Hypoxia-specific ultrasensitive detection of tumours and cancer cells in vivo. Nat Commun. 2015;6:5834.
77. Napp J, Behnke T, Fischer L, WÜRth C, Wottawa M, Katschinski DRM, Alves F, Resch-Genger U, Schäferling M. Targeted luminescent near-infrared

polymer-nanoprobes for in vivo imaging of tumor hypoxia. Anal Chem. 2011;83:9039–46.
78. Palmer GM, Fontanella AN, Zhang G, Hanna G, Fraser CL, Dewhirst MW. Optical imaging of tumor hypoxia dynamics. J Biomed Opt. 2010;15:7–066021.
79. Okuda K, Okabe Y, Kadonosono T, Ueno T, Youssif BG, Kizaka-Kondoh S, Nagasawa H. 2-Nitroimidazole-tricarbocyanine conjugate as a near-infrared fluorescent probe for in vivo imaging of tumor hypoxia. Bioconjug Chem. 2012;23:324–9.
80. Takahashi S, Piao W, Matsumura Y, Komatsu T, Ueno T, Terai T, Kamachi T, Kohno M, Nagano T, Hanaoka K. Reversible off–on fluorescence probe for hypoxia and imaging of hypoxia–normoxia cycles in live cells. J Am Chem Soc. 2012;134:19588–91.
81. Son A, Kawasaki A, Hara D, Ito T, Tanabe K. Phosphorescent ruthenium complexes with a nitroimidazole unit that image oxygen fluctuation in tumor tissue. Chemistry. 2015;21:2527–36.
82. Liu J, Liu Y, Bu W, Bu J, Sun Y, Du J, Shi J. Ultrasensitive nanosensors based on upconversion nanoparticles for selective hypoxia imaging in vivo upon near-infrared excitation. J Am Chem Soc. 2014;136:9701–9.
83. Komatsu H, Yoshihara K, Yamada H, Kimura Y, Son A, Nishimoto SI, Tanabe K. Ruthenium complexes with hydrophobic ligands that are key factors for the optical imaging of physiological hypoxia. Chemistry. 2013;19:1971–7.
84. Zhang S, Hosaka M, Yoshihara T, Negishi K, Iida Y, Tobita S, Takeuchi T. Phosphorescent light–emitting iridium complexes serve as a hypoxia-sensing probe for tumor imaging in living animals. Cancer Res. 2010;70:4490–8.
85. Gillies RJ. In vivo molecular imaging. J Cell Biochem Suppl. 2002;39:231–8.
86. Gallagher FA, Kettunen MI, Day SE, Hu D-E, Ardenkjær-Larsen JH, Jensen PR, Karlsson M, Golman K, Lerche MH, Brindle KM. Magnetic resonance imaging of pH in vivo using hyperpolarized 13C-labelled bicarbonate. Nature. 2008;453:940–3.
87. Engin K, Leeper DB, Cater JR, Thistlethwaite AJ, Tupchong L, McFarlane JD. Extracellular pH distribution in human tumours. Int J Hyperth. 1995;11:211–6.
88. Vaupel P, Kallinowski F, Okunieff P. Blood flow, oxygen and nutrient supply, and metabolic microenvironment of human tumors: a review. Cancer Res. 1989;49:6449–65.
89. Damaghi M, Wojtkowiak JW, Gillies RJ. pH sensing and regulation in cancer. Front Physiol. 2013;4:370.
90. van den Berg AP, Wike-Hooley JL, van den Berg-Blok AE, van der Zee J, Reinhold HS. Tumour pH in human mammary carcinoma. Eur J Cancer Clin Oncol. 1982;18:457–62.
91. Bicher HI, Hetzel FW, Sandhu TS, Frinak S, Vaupel P, O'Hara MD, O'Brien T. Effects of hyperthermia on normal and tumor microenvironment. Radiology. 1980;137:523–30.
92. Calderwood SK, Dickson JA. pH and tumor response to hyperthermia. Adv. Radiat. Biol. 1983;10:135–90.
93. Gallagher FA, Kettunen MI, Brindle KM. Imaging pH with hyperpolarized 13C. NMR Biomed. 2011;24:1006–15.
94. Jindal AK, Merritt ME, Suh EH, Malloy CR, Sherry AD, Kovács Z. Hyperpolarized 89Y complexes as pH sensitive NMR probes. J Am Chem Soc. 2010;132:1784–5.
95. Scholz DJ, Janich MA, Köllisch U, Schulte RF, Ardenkjaer-Larsen JH, Frank A, Haase A, Schwaiger M, Menzel MI. Quantified pH imaging with hyperpolarized 13C-bicarbonate. Magn Reson Med. 2015;73:2274–82.
96. Ward KM, Balaban RS. Determination of pH using water protons and chemical exchange dependent saturation transfer (CEST). Magn Reson Med. 2000;44:799.
97. Huang Y, Coman D, Ali MM, Hyder F. Lanthanide ion (III) complexes of 1,4,7,10-tetraazacyclododecane-1, 4, 7, 10-tetraaminophosphonate for dual biosensing of pH with chemical exchange saturation transfer (CEST) and biosensor imaging of redundant deviation in shifts (BIRDS). Contrast Media Mol Imaging. 2015;10:51–8.
98. Moon BF, Jones KM, Chen LQ, Liu P, Randtke EA, Howison CM, Pagel MD. A comparison of iopromide and iopamidol, two acidoCEST MRI contrast media that measure tumor extracellular pH. Contrast Media Mol Imaging. 2015;10:446–55.
99. Chen LQ, Randtke EA, Jones KM, Moon BF, Howison CM, Pagel MD. Evaluations of tumor acidosis within in vivo tumor models using parametric maps generated with AcidoCEST MRI. Mol Imaging Biol. 2015;17:488–96.
100. Chen LQ, Howison CM, Jeffery JJ, Robey IF, Kuo PH, Pagel MD. Evaluations of extracellular pH within in vivo tumors using acidoCEST MRI. Magn Reson Med. 2014;72:1408–17.
101. Longo DL, Busato A, Lanzardo S, Antico F, Aime S. Imaging the pH evolution of an acute kidney injury model by means of iopamidol, a MRI-CEST pH-responsive contrast agent. Magn Reson Med. 2013;70:859–64.
102. Longo DL, Sun PZ, Consolino L, Michelotti FC, Uggeri F, Aime S. A general MRI-CEST ratiometric approach for pH imaging: demonstration of in vivo pH mapping with iobitridol. J Am Chem Soc. 2014;136:14333–6.
103. Aime S, Delli Castelli D, Terreno E. Novel pH-reporter MRI contrast agents. Angew Chem Int Ed Engl. 2002;114:4510–2.
104. Chen Y, Yin Q, Ji X, Zhang S, Chen H, Zheng Y, Sun Y, Qu H, Wang Z, Li Y, Wang X, Zhang K, Zhang L, Shi J. Manganese oxide-based multifunctionalized mesoporous silica nanoparticles for pH-responsive

MRI, ultrasonography and circumvention of MDR in cancer cells. Biomaterials. 2012;33:7126–37.
105. Sheth VR, Li Y, Chen LQ, Howison CM, Flask CA, Pagel MD. Measuring in vivo tumor pHe with CEST-FISP MRI. Magn Reson Med. 2012;67:760–8.
106. Nwe K, Huang C-H, Tsourkas A. Gd-labeled glycol chitosan as a pH-responsive magnetic resonance imaging agent for detecting acidic tumor microenvironments. J Med Chem. 2013;56:7862–9.
107. Lee YJ, Kang HC, Hu J, Nichols JW, Jeon YS, Bae YH. pH-sensitive polymeric micelle-based pH probe for detecting and imaging acidic biological environments. Biomacromolecules. 2012;13:2945–51.
108. Crayton SH, Tsourkas A. pH-Titratable superparamagnetic iron oxide for improved nanoparticle accumulation in acidic tumor microenvironments. ACS Nano. 2011;5:9592–601.
109. Rivas C, Stasiuk GJ, Gallo J, Minuzzi F, Rutter GA, Long NJ. Lanthanide(III) complexes of Rhodamine-DO3A conjugates as agents for dual-modal imaging. Inorg Chem. 2013;52:14284–93.
110. Li Y, Wang Y, Yang S, Zhao Y, Yuan L, Zheng J, Yang R. Hemicyanine-based high resolution ratiometric near-infrared fluorescent probe for monitoring pH changes in vivo. Anal Chem. 2015;87:2495–503.
111. Doria F, Folini M, Grande V, Cimino-Reale G, Zaffaroni N, Freccero M. Naphthalene diimides as red fluorescent pH sensors for functional cell imaging. Org Biomol Chem. 2015;13:570–6.
112. Wang L, Fan Z, Zhang J, Changyi Y, Huang C, Gu Y, Xu Z, Tang Z, Lu W, Wei X. Evaluating tumor metastatic potential by imaging intratumoral acidosis via pH-activatable near-infrared fluorescent probe. Int J Cancer. 2015;136:E107–16.
113. Liu X-D, Xu Y, Sun R, Xu Y-J, Lu J-M, Ge J-F. A coumarin–indole-based near-infrared ratiometric pH probe for intracellular fluorescence imaging. Analyst. 2013;138:6542–50.
114. Ding C, Tian Y. Gold nanocluster-based fluorescence biosensor for targeted imaging in cancer cells and ratiometric determination of intracellular pH. Biosens Bioelectron. 2015;65:183–90.
115. Liu X, Chen Q, Yang G, Zhang L, Liu Z, Cheng Z, Zhu X. Magnetic nanomaterials with near-infrared pH-activatable fluorescence via iron-catalyzed AGET ATRP for tumor acidic microenvironment imaging. J Mater Chem B. 2015;3:2786–800.
116. Wang Y, Zhou K, Huang G, Hensley C, Huang X, Ma X, Zhao T, Sumer BD, Deberardinis RJ, Gao J. A nanoparticle-based strategy for the imaging of a broad range of tumors by nonlinear amplification of microenvironment signals. Nat Mater. 2014;13:204–12.
117. Ko JY, Park S, Lee H, Koo H, Kim MS, Choi K, Kwon IC, Jeong SY, Kim K, Lee DS. pH-sensitive nanoflash for tumoral acidic pH imaging in live animals. Small. 2010;6:2539–44.
118. Li C, Xia J, Wei X, Yan H, Si Z, Ju S. pH-activated near-infrared fluorescence nanoprobe imaging tumors by sensing the acidic microenvironment. Adv Funct Mater. 2010;20:2222–30.
119. Dong C, Liu Z, Zhang L, Guo W, Li X, Liu J, Wang H, Chang J. pHe-induced charge-reversible NIR fluorescence nanoprobe for tumor-specific imaging. ACS Appl Mater Interfaces. 2015;7:7566–75.
120. Lemon CM, Curtin PN, Somers RC, Greytak AB, Lanning RM, Jain RK, Bawendi MG, Nocera DG. Metabolic tumor profiling with pH, oxygen, and glucose chemosensors on a quantum dot scaffold. Inorg Chem. 2014;53:1900–15.
121. Dennis AM, Rhee WJ, Sotto D, Dublin SN, Bao G. Quantum dot–fluorescent protein FRET probes for sensing intracellular pH. ACS Nano. 2012;6:2917–24.
122. Wu W, Aiello M, Zhou T, Berliner A, Banerjee P, Zhou S. In-situ immobilization of quantum dots in polysaccharide-based nanogels for integration of optical pH-sensing, tumor cell imaging, and drug delivery. Biomaterials. 2010;31:3023–31.
123. Shirmanova MV, Druzhkova IN, Lukina MM, Matlashov ME, Belousov VV, Snopova LB, Prodanetz NN, Dudenkova VV, Lukyanov SA, Zagaynova EV. Intracellular pH imaging in cancer cells in vitro and tumors in vivo using the new genetically encoded sensor SypHer2. Biochim Biophys Acta. 2015;1850:1905–11.
124. Tantama M, Hung YP, Yellen G. Imaging intracellular pH in live cells with a genetically encoded red fluorescent protein sensor. J Am Chem Soc. 2011;133:10034–7.
125. Huang G, Si Z, et al. Dextran based pH-sensitive near-infrared nanoprobe for in vivo differential-absorption dual-wavelength photoacoustic imaging of tumors. J Mater Chem. 2012;22:22575–81.
126. Flavell RR, Truillet C, Regan MK, Ganguly T, Blecha JE, Kurhanewicz J, Vanbrocklin HF, Keshari KR, Chang CJ, Evans MJ, Wilson DM. Caged [(18) F]FDG glycosylamines for imaging acidic tumor microenvironments using positron emission tomography. Bioconjug Chem. 2016;27:170–8.
127. Andreev OA, Engelman DM, Reshetnyak YK. pH-sensitive membrane peptides (pHLIPs) as a novel class of delivery agents. Membr Biol. 2010;27:341–52.
128. Andreev OA, Engelman DM, Reshetnyak YK. Targeting diseased tissues by pHLIP insertion at low cell surface pH. Front Physiol. 2014;5:97.
129. Adochite R-C, Moshnikova A, Carlin SD, Guerrieri RA, Andreev OA, Lewis JS, Reshetnyak YK. Targeting breast tumors with pH (low) insertion peptides. Mol Pharm. 2014;11:2896–905.
130. Cruz-Monserrate Z, Roland CL, Deng D, Arumugam T, Moshnikova A, Andreev OA, Reshetnyak YK, Logsdon CD. Targeting pancreatic ductal adenocarcinoma acidic microenvironment. Sci. Rep. 2014;4:4410/1–8.
131. Loja MN, Luo Z, Greg Farwell D, Luu QC, Donald PJ, Amott D, Truong AQ, Gandour-Edwards RF,

Nitin N. Optical molecular imaging detects changes in extracellular pH with the development of head and neck cancer. Int J Cancer. 2013;132:1613–23.
132. Macholl S, Morrison MS, Iveson P, Arbo BE, Andreev OA, Reshetnyak YK, Engelman DM, Johannesen E. In vivo pH imaging with 99mTc-pHLIP. Mol Imaging Biol. 2012;14:725–34.
133. Rothberg JM, Sameni M, Moin K Live-cell imaging of tumor proteolysis: impact of cellular and noncellular microenvironment. Biochim Biophys Acta. 2012;1824:123–32.
134. Mason SD, Joyce JA. Proteolytic networks in cancer. Trends Cell Biol. 2011;21:228–37.
135. Matusiak N, van Waarde A, Bischoff R, Oltenfreiter R, van de Wiele C, Dierckx RA, Elsinga PH. Probes for non-invasive matrix metalloproteinase-targeted imaging with PET and SPECT. Curr Pharm Des. 2013;19:4647–72.
136. Narunsky L, Oren R, Bochner F, Neeman M. Imaging aspects of the tumor stroma with therapeutic implications. Pharmacol Ther. 2014;141:192–208.
137. Chen H, Zhang X, Dai S, Ma Y, Cui S, Achilefu S, Gu Y. Multifunctional gold nanostar conjugates for tumor imaging and combined photothermal and chemo-therapy. Theranostics. 2013;3:633–49. 17 pp
138. D'Alessio S, Ferrari G, Cinnante K, et al. Tissue inhibitor of metalloproteinases-2 binding to membrane-type 1 matrix metalloproteinase induces MAPK activation and cell growth by a non-proteolytic mechanism. J Biol Chem. 2008;283:87–99.
139. Sato H, Takino T, Okada Y, Cao J, Shinagawa A, Yamamoto E, Seiki M. A matrix metalloproteinase expressed on the surface of invasive tumour cells. Nature. 1994;370:61–5.
140. Uekita T, Itoh Y, Yana I, Ohno H, Seiki M. Cytoplasmic tail-dependent internalization of membrane-type 1 matrix metalloproteinase is important for its invasion-promoting activity. J Cell Biol. 2001;155:1345–56.
141. Matusiak N, Castelli R, Tuin AW, Overkleeft HS, Wisastra R, Dekker FJ, Prély LM, Bischoff RPH, van Waarde A, Dierckx RAJO. A dual inhibitor of matrix metalloproteinases and a disintegrin and metalloproteinases, [18F]FB-ML5, as a molecular probe for non-invasive MMP/ADAM-targeted imaging. . Bioorganic. Med Chem. 2015;23:192–202.
142. Altiparmak BL, Yurt F, Citak A. Design of radiolabeled gelatinase inhibitor peptide (99mTc-CLP) and evaluation in rats. Appl Radiat Isot. 2014;89:130–3.
143. Efrem Mebrahtu AZ, Hur MA, Laforest R, Lapi SE. Initial characterization of a dually radiolabeled peptide for simultaneous monitoring of protein targets and enzymatic activity. Nucl Med Biol. 2013;40:190.
144. Da Rocha Gomes S, Miguel J, Azéma L, Eimer S, Ries C, Dausse E, Loiseau H, Allard M, Toulmé JJ. 99mTc-MAG3-Aptamer for imaging human tumors associated with high level of matrix Metalloprotease-9. Bioconjug Chem. 2012;23:2192–200.
145. Kondo N, Temma T, Shimizu Y, Watanabe H, Higano K, Takagi Y, Ono M, Saji H. Miniaturized antibodies for imaging membrane type-1 matrix metalloproteinase in cancers. Cancer Sci. 2013;104:495–501.
146. van Duijnhoven SMJR, Marc S, Nicolay K, Gruell H. In vivo biodistribution of radiolabeled MMP-2/9 activatable cell-penetrating peptide probes in tumor-bearing mice. Contrast Media Mol Imaging. 2015;10:59–66.
147. van Duijnhoven SMJR, Marc S, Nicolay K, Gruell H. Tumor targeting of MMP-2/9 activatable cell-penetrating imaging probes is caused by tumor-independent activation. J Nucl Med. 2011;52:279–86.
148. Zhao T, Harada H, Teramura Y, Tanaka S, Itasaka S, Morinibu A, Shinomiya K, Zhu Y, Hanaoka H, Iwata H, Saji H, Hiraoka M. A novel strategy to tag matrix metalloproteinases-positive cells for in vivo imaging of invasive and metastatic activity of tumor cells. J Control Release. 2010;144:109–14.
149. Al Rawashdeh W, Arns S, Gremse F, Ehling J, Knüchel-Clarke R, Kray S, Spöler F, Kiessling F, Lederle W. Optical tomography of MMP activity allows a sensitive noninvasive characterization of the invasiveness and angiogenesis of SCC xenografts. Neoplasia. 2015;16:235–46.
150. Wang Y, Lin T, Zhang W, Jiang Y, Jin H, He H, Yang VC, Chen Y, Huang Y. A prodrug-type, MMP-2-targeting nanoprobe for tumor detection and imaging. Theranostics. 2015;5:787–95.
151. Kawano T, Murata M, Piao JS, Narahara S, Hamano N, Kang JH, Hashizume M. Systemic delivery of protein nanocages bearing CTT peptides for enhanced imaging of MMP-2 expression in metastatic tumor models. Int J Mol Sci. 2015;16:148–58.
152. Chen WH, Xu XD, Jia HZ, Lei Q, Luo GF, Cheng SX, Zhuo RX, Zhang XZ. Therapeutic nanomedicine based on dual-intelligent functionalized gold nanoparticles for cancer imaging and therapy in vivo. Biomaterials. 2013;34:8798–807.
153. Zhang X, Bresee J, Fields GB, Barry Edwards W. Near-infrared triple-helical peptide with quenched fluorophores for optical imaging of MMP-2 and MMP-9 proteolytic activity in vivo. Bioorg Med Chem Lett. 2014;24:3786–90.
154. Shimizu Y, Temma T, Hara I, Makino A, Kondo N, Ozeki E, Ono M, Saji H. In vivo imaging of membrane type-1 matrix metalloproteinase with a novel activatable near-infrared fluorescence probe. Cancer Sci. 2014;105:1056–62.
155. Myochin T, Hanaoka K, Iwaki S, Ueno T, Komatsu T, Terai T, Nagano T, Urano Y. Development of a series of near-infrared dark quenchers based on Si-rhodamines and their application to fluorescent probes. J Am Chem Soc. 2015;137:4759–65.
156. Rood MT, Raspe M, ten Hove JB, Jalink K, Velders AH, van Leeuwen FW. MMP-2/9-specific

activatable lifetime imaging agent. Sensors (Basel). 2015;15:11076–91.
157. Levi J, Kothapalli SR, Bohndiek S, Yoon JK, Dragulescu-Andrasi A, Nielsen C, Tisma A, Bodapati S, Gowrishankar G, Yan X, Chan C, Starcevic D, Gambhir SS. Molecular photoacoustic imaging of follicular thyroid carcinoma. Clin Cancer Res. 2013;19:1494–502.
158. Waschkau B, Faust A, Schäfers M, Bremer C. Performance of a new fluorescence-labeled MMP inhibitor to image tumor MMP activity in vivo in comparison to an MMP-activatable probe. Contrast Media Mol Imaging. 2013;8:1–11.
159. Gallo J, Kamaly N, Lavdas I, Stevens E, Nguyen QD, Wylezinska-Arridge M, Aboagye EO, Long NJ. CXCR4-targeted and MMP-responsive iron oxide nanoparticles for enhanced magnetic resonanceimaging. Angew Chem Int Ed Engl. 2014;53:9550–4.
160. Crisp JL, Savariar EN, Glasgow HL, Ellies LG, Whitney MA, Tsien RY. Dual targeting of integrin avb3 and matrix Metalloproteinase-2 for optical imaging of tumors and chemotherapeutic delivery. Mol Cancer Ther. 2014;13:1514–25.
161. Ansari C, Tikhomirov GA, Hong SH, Falconer RA, Loadman PM, Gill JH, Castaneda R, Hazard FK, Tong L, Lenkov OD, Felsher DW, Rao J, Daldrup-Link HE. Development of novel tumor-targeted theranostic nanoparticles activated by membrane-type matrix metalloproteinases for combined cancer magnetic resonance imaging and therapy. Small. 2014;10:566–75.
162. Matsuo K, Kamada R, Mizusawa K, Imai H, Takayama Y, Narazaki M, Matsuda T, Takaoka Y, Hamachi I. Specific detection and imaging of enzyme activity by signal-amplifiable self-assembling 19F MRI probes. Chem Eur J. 2013;19:12875–83.
163. Reiser J, Adair B, Reinheckel T. Specialized roles for cysteine cathepsins in health and disease. J Clin Invest. 2010;120:3421–31.
164. Mohamed MM, Sloane BF. Cysteine cathepsins: multifunctional enzymes in cancer. Nat Rev Cancer. 2006;6:764–75.
165. Palermo C, Joyce JA. Cysteine cathepsin proteases as pharmacological targets in cancer. Trends Pharmacol Sci. 2008;29:22–8.
166. Loeser R, Bergmann R, Frizler M, Mosch B, Dombrowski L, Kuchar M, Steinbach J, Guetschow M, Pietzsch J. Synthesis and radiopharmacological characterisation of a Fluorine-18-labelled Azadipeptide nitrile as a potential PET tracer for in vivo imaging of cysteine cathepsins. ChemMedChem. 2013;8:1330–44.
167. Ren G, Blum G, Verdoes M, Liu H, Syed S, Edgington LE, Gheysens O, Miao Z, Jiang H, Gambhir SS, Bogyo M, Cheng Z. Non-invasive imaging of cysteine cathepsin activity in solid tumors using a 64Cu-labeled activity-based probe. PLoS One. 2011;6:e28029.
168. Shi W, Ogbomo SM, Wagh NK, Zhou Z, Jia Y, Brusnahan SK, Garrison JC. The influence of linker length on the properties of cathepsin S cleavable 177Lu-labeled HPMA copolymers for pancreatic cancer imaging. Biomaterials. 2014;35:5760–70.
169. Haris M, Singh A, Mohammed I, Ittyerah R, Nath K, Nanga RPR, Debrosse C, Kogan F, Cai K, Poptani H, Reddy D, Hariharan H, Reddy R. In vivo magnetic resonance imaging of tumor protease activity. Sci Rep. 2014;4:6081.
170. Fujii T, Kamiya M, Urano Y. In vivo imaging of Intraperitoneally disseminated tumors in model mice by using activatable fluorescent small-molecular probes for activity of cathepsins. Bioconjug Chem. 2014;25:1838–46.
171. Ryu JH, Na JH, Ko HK, You DG, Park S, Jun E, Yeom HJ, Seo DH, Park JH, Jeong SY, Kim I-S, Kim B-S, Kwon IC, Choi K, Kim K. Non-invasive optical imaging of cathepsin B with activatable fluorogenic nanoprobes in various metastatic models. Biomaterials. 2014;35:2302–11.
172. Kisin-Finfer E, Ferber S, Blau R, Satchi-Fainaro R, Shabat D. Synthesis and evaluation of new NIR-fluorescent probes for cathepsin B: ICT versus FRET as a turn-ON mode-of-action. Bioorg Med Chem Lett. 2014;24:2453–8.
173. Tian R, Li M, Wang J, Yu M, Kong X, Feng Y, Chen Z, Li Y, Huang W, Wu W, Hong Z. An intracellularly activatable, fluorogenic probe for cancer imaging. Org Biomol Chem. 2014;12:5365–74.
174. Cuneo KC, Mito JK, Javid MP, Ferrer JM, Kim Y, Lee WD, Bawendi MG, Brigman BE, Kirsch DG. Imaging primary mouse sarcomas after radiation therapy using cathepsin-activatable fluorescent imaging agents. Int J Radiat Oncol Biol Phys. 2013;86:136–42.
175. ABD-Elgaliel WR, Cruz-Monserrate Z, Logsdon CD, Tung C-H. Molecular imaging of Cathepsin E-positive tumors in mice using a novel protease-activatable fluorescent probe. Mol BioSyst. 2011;7:3207–13.
176. Hu H-Y, Vats D, Vizovisek M, Kramer L, Germanier C, Wendt KU, Rudin M, Turk B, Plettenburg O, Schultz C. In vivo imaging of mouse tumors by a lipidated cathepsin substrate. Angew Chem Int Ed Engl. 2014;53:7669–73.
177. Verdoes M, Edgington LE, Scheeren FA, Leyva M, Blum G, Weiskopf K, Bachmann MH, Ellman JA, Bogyo M. A nonpeptidic cathepsin S activity-based probe for noninvasive optical imaging of tumor-associated macrophages. Chem Biol. 2012;19:619–28.
178. Goodman SL, Picard M. Integrins as therapeutic targets. Trends Pharmacol Sci. 2012;33:405–12.
179. Goswami S. Importance of integrin receptors in the field of pharmaceutical, medical science. Adv Biol Chem. 2013;3:224–52. 29 pp

180. Danhier F, Breton AL, Préat VR. RGD-based strategies to target alpha (v) beta (3) integrin in cancer therapy and diagnosis. Mol Pharm. 2012;9:2961–73.
181. Guo J, Lang L, Hu S, Guo N, Zhu L, Sun Z, Ma Y, Kiesewetter DO, Niu G, Xie Q, Chen X. Comparison of three dimeric 18F-AlF-NOTA-RGD tracers. Mol Imaging Biol. 2014;16:274–83.
182. Mena E, Owenius R, Turkbey B, Sherry R, Bratslavsky G, Macholl S, Miller MP, Somer EJ, Lindenberg L, Adler S, Shih J, Choyke P, Kurdziel K. [18F]Fluciclatide in the in vivo evaluation of human melanoma and renal tumors expressing αvβ3 and αvβ5 integrins. Eur J Nucl Med Mol Imaging. 2014;41:1879–88.
183. Haubner R, Rangger C, Virgolini IJ, Maschauer S, Prante O, Einsiedel J, Gmeiner P, Eder IE. H-CRRETAWAC-OH, a lead structure for the development of radiotracer targeting integrin α5β1? Biomed Res Int. 2014;2014:243185.
184. Bao X, Wang M-W, Xu J-Y, Zheng Y-J, Jiang J-J, Zhang Y-J. Biodistribution in healthy KM mice and micro PET/CT imaging in U87MG tumor-bearing nude mice of a new 18F-labeled cyclic RGD dimer. Zhongguo Aizheng Zazhi. 2013;23:408–12.
185. Hackel BJ, Kimura RH, Miao Z, Liu H, Sathirachinda A, Cheng Z, Chin FT, Gambhir SS. 18F-fluorobenzoate-labeled cystine knot peptides for PET imaging of integrin αvβ6. J Nucl Med. 2013;54:1101–5.
186. Beer AJ, Pelisek J, Heider P, Reeps C, Eckstein HH, Saraste A, Metz S, Seidl S, Kessler H, Wester H-J, Schwaiger M. PET/CT imaging of integrin αvβ3 expression in human carotid atherosclerosis. JACC Cardiovasc Imaging. 2014;7:178–87.
187. Bryden F, Rosca EV, Boyle RW. PET/PDT theranostics: synthesis and biological evaluation of a peptide-targeted Ga-68 porphyrin. Dalton Trans. 2014;44:4925–32.
188. McBride WJ, D'Souza CA, Sharkey RM, Karacay H, Rossi EA, Chang C-H, Goldenberg DM. Improved F-18 labeling of peptides with a fluoride-aluminum-chelate complex. Bioconjug Chem. 2010;21:1331–40.
189. WJ MB, Sharkey RM, Goldenberg DM, McBride WJ. Radiofluorination using aluminum-fluoride (Al18F). EJNMMI Res. 2013;3:36.
190. Hausner SH, Bauer N, Sutcliffe JL. In vitro and in vivo evaluation of the effects of aluminum [18F] fluoride radiolabeling on an integrin αvβ6-specific peptide. Nucl Med Biol. 2014;41:43–50.
191. Bejot R, Goggi J, Moonshi SS, Robins EG. A practical synthesis of [18F]FtRGD: an angiogenesis biomarker for PET. J Label Compd Radiopharm. 2013;56:42–9.
192. Singh AN, McGuire MJ, Li S, Hao G, Kumar A, Sun X, Brown KC. Dimerization of a phage-display selected peptide for imaging of αvβ6- integrin: two approaches to the multivalent effect. Theranostics. 2014;4:745–60.
193. Hu LY, Bauer N, Knight LM, Li Z, Liu S, Anderson CJ, Conti PS, Sutcliffe JL. Characterization and evaluation of (64)Cu-labeled A20FMDV2 conjugates for imaging the integrin αvβ 6. Mol Imaging Biol. 2014;16:567–77.
194. Shokeen M, Zheleznyak A, Wilson JM, Jiang M, Liu R, Ferdani R, Lam KS, Schwarz JK, Anderson CJ. Molecular imaging of very late antigen-4 (α4β1 integrin) in the premetastatic niche. J Nucl Med. 2012;53:779–86.
195. Ortiz-Arzate Z, Santos-Cuevas CL, Ocampo-Garcia BE, Ferro-Flores G, Garcia-Becerra R, Estrada G, Gomez-Argumosa E, Izquierdo-Sanchez V. Kit preparation and biokinetics in women of 99mTc-EDDA/HYNIC-E-[c(RGDfK)]2 for breast cancer imaging. Nucl Med Commun. 2014;35:423–32.
196. Li F, Song Z, Li Q, Wu J, Wang J, Xie C, Tu C, Wang J, Huang X, Lu W. Molecular imaging of hepatic stellate cell activity by visualization of hepatic integrin αvβ3 expression with SPECT in rat. Hepatology. 2011;54:1020–30.
197. Liu Z, Liu H, Ma T, Sun X, Shi J, Jia B, Sun Y, Zhan J, Zhang H, Zhu Z, Wang F. Integrin αvβ6-targeted SPECT imaging for pancreatic cancer detection. J Nucl Med. 2014;55:989–94.
198. Zhu X, Li J, Hong Y, Kimura RH, Ma X, Liu H, Qin C, Hu X, Hayes TR, Benny P, Gambhir SS, Cheng Z. 99mTc-Labeled cystine knot peptide targeting integrin αvβ6 for tumor SPECT imaging. Mol Pharm. 2014;11:1208–17.
199. Ueda M, Fukushima T, Ogawa K, Kimura H, Ono M, Yamaguchi T, Ikehara Y, Saji H. Synthesis and evaluation of a radioiodinated peptide probe targeting αvβ6 integrin for the detection of pancreatic ductal adenocarcinoma. Biochem Biophys Res Commun. 2014;445:661–6.
200. John AE, Luckett JC, Tatler AL, Awais RO, Desai A, Habgood A, Ludbrook S, Blanchard AD, Perkins AC, Jenkins RG, Marshall JF. Preclinical SPECT/CT imaging of αvβ6 integrins for molecular stratification of idiopathic pulmonary fibrosis. J Nucl Med. 2013;54:2146–52.
201. Gao D, Gao L, Zhang C, Liu H, Jia B, Zhu Z, Wang F, Liu Z. A near-infrared phthalocyanine dye-labeled agent for integrin αvβ6-targeted theranostics of pancreatic cancer. Biomaterials. 2015;53:229–38.
202. Moore SJ, Hayden GMG, Bergen JM, Su YS, Rayburn H, Scott MP, Cochran JR. Engineered knottin peptide enables noninvasive optical imaging of intracranial medulloblastoma. Proc Natl Acad Sci U S A. 2013;110:14598–603.
203. Shi H, Liu J, Geng J, Tang BZ, Liu B. Specific detection of integrin αvβ3 by light-up bioprobe with aggregation-induced emission characteristics. J Am Chem Soc. 2012;134:9569–72.
204. Kossodo S, Pickarski M, Lin S-A, Gleason A, Gaspar R, Buono C, Ho G, Blusztajn A, Cuneo G, Zhang J, Jensen J, Hargreaves R, Coleman P, Hartman G, Rajopadhye M, Duong LT, Sur C, Yared W, Peterson

J, Bednar B. Dual in vivo quantification of integrin-targeted and protease-activated agents in cancer using fluorescence molecular tomography (FMT). Mol Imaging Biol. 2010;12:488–99.
205. Satpati D, Hausner SH, Bauer N, Sutcliffe JL. Cerenkov luminescence imaging of αvβ6 integrin expressing tumors using 90Y-labeled peptides. J Label Compd Radiopharm. 2014;57:558–65.
206. Kawamura W, Miura Y, Kokuryo D, Toh K, Yamada N, Nomoto T, Matsumoto Y, Sueyoshi D, Liu X, Aoki I. Density-tunable conjugation of cyclic RGD ligands with polyion complex vesicles for the neovascular imaging of orthotopic glioblastomas. Sci Technol Adv Mater. 2015;16:1–13.
207. Yan C, Wu Y, Feng J, Chen W, Liu X, Hao P, Yang R, Zhang J, Lin B, Xu Y, Liu R. Anti-αvβ3 antibody guided three-step pretargeting approach using magnetoliposomes for molecular magnetic resonance imaging of breast cancer angiogenesis. Int J Nanomedicine. 2013;8:245–55.